Chemical Engineering Journal 520 (2025) 166441

Contents lists available at ScienceDirect

Chemical Engineering Journal

journal homepage: www.elsevier.com/locate/cej

Thermally insulating mats based on electrospun fibers with bioinspired nano-groove surface structure

Daniel P. Ura [a], Piotr K. Szewczyk [a], Gregory Parisi [b], Andrzej Osak [c], Bartosz Puzio [d], Jan Wrona [c], Il-Doo Kim [e], Urszula Stachewicz [a,*]

[a] Faculty of Metals Engineering and Industrial Computer Science, AGH University of Krakow, Mickiewicz 30, 30-065 Kraków, Poland
[b] Department of Mechanical Engineering and Applied Mechanics, School of Engineering and Applied Sciences, University of Pennsylvania, 220 South 33rdrd Street, Philadelphia, PA 19104-6315, United States
[c] Faculty of Environmental Engineering and Energy, Cracow University of Technology, Warszawska 24, 31-155, Kraków, Poland
[d] Faculty of Geology, Geophysics, and Environmental Protection, AGH University of Krakow, Mickiewicz 30, 30-065 Kraków, Poland
[e] Department of Materials Science and Engineering, Korea Advanced Institute of Science and Technology (KAIST), Daejeon, Republic of Korea

ARTICLE INFO

Keywords:
Biomimetics
Nature-inspired materials
Polymer fibers
Thermal properties
Nanogrooved structure
Electrospinning

ABSTRACT

Heating and heat retention in buildings account for over 50 % of total energy costs, emphasizing the urgent need not only for advanced thermal insulation materials but also for nature-inspired design strategies to enhance energy efficiency and address the global energy crisis. In this study, we present a one-step fabrication method that improves both thermal insulation efficiency and the mechanical performance of polymer fiber mats. By leveraging bioinspired design, we successfully fabricate nanogroove fibers by precisely controlling humidity during in-situ electrospinning. This approach mimics the nanogroove topography of Old Man Cactus hair, enabling a simple yet effective method to regulate the nanoscale morphology of fibers. The resulting nanogroove fibers exhibit a substantial ~10 % reduction in surface temperature compared to conventional insulation coatings when applied to hot water pipes. Remarkably, our nanogroove fibrous coatings achieve 25 % higher energy savings per unit area and approximately 29 times higher per gram of material mass than commercial rubber insulation materials. This study highlights the critical role of nanoscale surface morphology engineering, particularly in the facile fabrication of nanogroove structures, in mitigating energy and heat loss during thermal transport processes. Based on the unique advantages of humidity-controlled polymer fiber architectures, this approach enables the development of flexible, high-performance thermal insulation materials, opening new avenues for versatile applications across various fields.

1. Introduction

With the rapid expansion of the global population and concerns over environmental sustainability, the energy crisis has become one of the most critical matters of our times [1]. Heating and heat retention in buildings account for more than 50 % of total energy costs [2]. As a result, improving thermal management through thermal insulation coatings is a key strategy for developing energy-efficient solutions. A straightforward example is the insulation used in indoor hot water circulation systems worldwide. However, current pipe systems can lose up to 10–30 % of their heat, causing an enormous economic burden for societies and impacting the environment [3]. Conventional water pipe insulation is composed of rubber, mineral, and glass wools or highly porous polymer foams, designed to minimize heat loss, thus saving energy consumption by 4–5 % annually [4]. Here, the effectiveness of pipe insulation is influenced by factors such as thickness (ranging from 6 to 200 mm), porosity, density, and, critically, the nanostructure of the materials [5,6]. A material's ability to resist heat conduction, along with its structural design, plays a vital role in insulation efficiency by trapping heat and preventing its escape, thereby enhancing overall heat retention [6]. Improving the efficiency of insulation materials can be achieved through various strategies. Increasing material porosity enhances thermal performance but often compromises its mechanical strength [7]. Another approach involves incorporating non-conductive nanoparticles, modifying the molecular structure, or introducing nanoporous or nanorough surfaces to precisely tailor thermal properties

* Corresponding author.
E-mail address: ustachew@agh.edu.pl (U. Stachewicz).

https://doi.org/10.1016/j.cej.2025.166441
Received 10 May 2025; Received in revised form 28 June 2025; Accepted 24 July 2025
Available online 25 July 2025

[8,9].

Animals and plants have evolved unique and effective thermal insulation mechanisms [10]. For example, polar bears and penguins possess specialized hairs or feathers, enabling them to regulate body temperatures in extreme conditions [11,12]. Similarly, in the plant kingdom, various adaptive strategies have evolved [10]. For instance, cacti have evolved unique structural and physiological attributes to thrive in desert environments [13]. One key factor in their ability to endure heat and minimize water loss is the thickness of their cuticle. Additionally, cacti spines serve multiple functions, including water harvesting, defense against predators, moisture collection from the air, and temperature regulation of the stem surface during the day [14]. The Old Man Cactus (Oreocereus trolli or *Cephalocereus senilis*) stands out not only for its spines but also for having the highest density of hair-like structures (trichomes) among cacti species [15]. While the precise function of cacti hairs is still not well examined, they are believed to provide insulating function by shielding the central part of the plant from sunlight, heat, and extreme temperature fluctuations in the desert. Keeley et al. demonstrated that the hairy form of *Tephrocactus floccosus* maintains a subepidermal temperature for three hours longer than its hairless counterpart, effectively reducing heat loss [13].

Electrospinning is a widely used technique for producing nano- and microscale fibers from various materials, including polymers, ceramics, and composites [16–18]. The basic principle of this method involves using an electric field to draw a polymer solution toward a grounded collector, where electrohydrodynamic phenomena lead to the formation of ultrafine electrospun continuous fibers [19]. Electrospinning parameters such as relative humidity (RH), play a crucial role in controlling surface morphology of individual fibers, enabling the formation of nanopores or grooves [20–22]. Compared to other fiber fabrication methods such as melt blowing or air-jet spinning, electrospinning allows precise tuning of the surface and structural properties of polymeric materials at the nanoscale during their production [23,24]. A key advantage of electrospinning is its scalability, which can be achieved through multiple nozzles, needleless, centrifugal force, or free surface systems [25]. With the growing interest in polymer fibers for thermal insulation, electrospinning has emerged as one of the most promising techniques for the commercialization of advanced insulation materials [26]. Polycarbonate (PC), an amorphous thermoplastic polymer, is particularly suitable for effective thermal insulation due to its high melting point (~288 °C), superior impact resistance, inherent flame resistance, and good mechanical performance [27]. Additionally, PC is chemically resistant to acids, neutral and acid salt solutions, greases, oils, detergents, and alcohols, and notably, it is fully recyclable [28].

In this study, we developed electrospun polymer fibers with high roughness and sufficient mechanical strength, biomimicking the hair of the Old Man Cactus, for use as a highly robust thermal insulation membrane. We demonstrated a one-step fabrication process via humidity-controlled electrospinning, enabling the production of non-woven fiber mats with customized thermal insulation properties. Experimental and computational analyses confirmed that fiber roughness, specifically nanogroove surface morphology, significantly enhances heat insulation by trapping air, thereby reducing thermal conductivity. Remarkably, our nanogroove fibrous mats achieved lower thermal conductivity values compared to commercially used rubber-based materials for pipe insulation. The low thickness and lightweight characteristics of our membranes offer significant advantages for practical applications where insulation layer dimensions are critical. Our bioinspired fibrous mats, optimized for superior thermal insulation, exhibit exceptional mechanical stability, lightweight, and desirable thermal properties, highlighting their potential for addressing global challenges such as energy loss and heat dissipation during transport.

2. Results and discussion

2.1. Investigation of Cephalocereus Senilis cactus hairs

Cacti are among the few plants that can endure drought conditions and high temperatures due to their internal and external structure. The role of cactus hair remains relatively unexplored; however, they serve as insulation, shielding the plant's inner core from the sun's intense heat and the temperature fluctuations typical of desert environments. Natural old man cactus (*Cephalocereus senilis*) hairs were collected and analyzed to serve as a basis for our biomimetic design (Fig. S1). As can be seen, the plant is covered with hair called trichomes and spines, which are characteristic of *Cephalocereus senilis* [29]. *We* extracted an areole from the cactus skin (Fig. S1A-E). The thickness and the pore size of the hairy layer in the cactus were determined, being 0.91 ± 0.23 and 0.08 cm ± 0.05 cm, respectively. Using scanning electron microscopy (SEM), the surface of the hairs was examined, showing characteristic grooves on the surface (Fig. S1F) and the average cactus hair diameter of 20.01 ± 5.05 μm.

Upon examination of the cactus hair, notable porosity is evident in the hair layer, with apparent variations in pore size (Fig. S1C). This suggests that one of the functions of the hairy layer is thermal insulation. We notice that cactus hairs have a rough, nanogroove surface, likely influencing heat transfer by inducing perturbations in the heat velocity profile [30]. Previously, Guen et al. showed that surface roughness at the nanoscale is meaningful in heat-conduction material [31]. Alternating the roughness of a material significantly changes the heat conduction path, consequently, its thermal conductivity [32]. Interestingly, nanoscale surface roughness can trap air gas molecules in grooves, lowering material's thermal conductivity [33]. In the case of cactus hair, nanogrooves on the surface serve as a key mechanism for temperature retention in the cactus stem.

2.2. Fabrication and characterization of the cactus-inspired polymer fibers

A schematic diagram of the strategy for manufacturing cactus-inspired fibrous mats for thermal insulation application is shown in Fig. 1. We successfully electrospun polymer fibers and mats with two types of surface morphology - smooth fiber (sF) and nanogrooved fiber (ngF), respectively (Fig. 2A, B and S2). These morphologies were achieved by adjusting RH during electrospinning - 60 % RH for sF and 30 % RH for ngF. The average fiber diameter (D_f) of sF and ngF was around 6.35 ± 0.90 and 5.17 ± 0.72 μm (Fig. S2). Additionally, fibers were cut using a focused ion beam (FIB) to investigate the cross-section geometry and internal structure of the produced fibers, which were further used to create the 3D reconstructions (Fig. 1A, B and S3). 3D tomography revealed voids with 92 ± 38 nm diameter inside sF fibers, with internal porosity around 11 %. For ngFs, the internal structure was solid (Fig. S3A, B). Investigation of individual fiber contour geometry investigation showed a circularity of 0.87 ± 0.01 for sF and 0.64 ± 0.04 for ngF (Fig. S3C). Using atomic force microscopy (AFM), we determined the average surface roughness (R_a) of single fibers: 20 ± 2 nm for sF, 119 ± 27 nm for ngF, and 131 ± 17 nm for cactus hair, respectively (Fig. 2C, D, E). All results with statistical significance among each group were summarized in Table S1.

Following this bioinspired design, we have successfully developed polymer fibers with a nanogroove structure (ngF). In this study, we compared it with - smooth fiber (sF) (Fig. 2A, B) to verify the effect of fiber roughness on preventing heat loss or maintaining a stable temperature. The nanogroove morphology of our fibers was attributed to differences in the solvent's evaporation dynamics in the polymer solution, controlled by the RH during electrospinning (Fig. 2B). At high RH, water can be absorbed and/or penetrate the polymer jet, leading to surface grooves, pores, and/or voids inside the fiber structure [34]. A more detailed discussion regarding surface morphology and groove

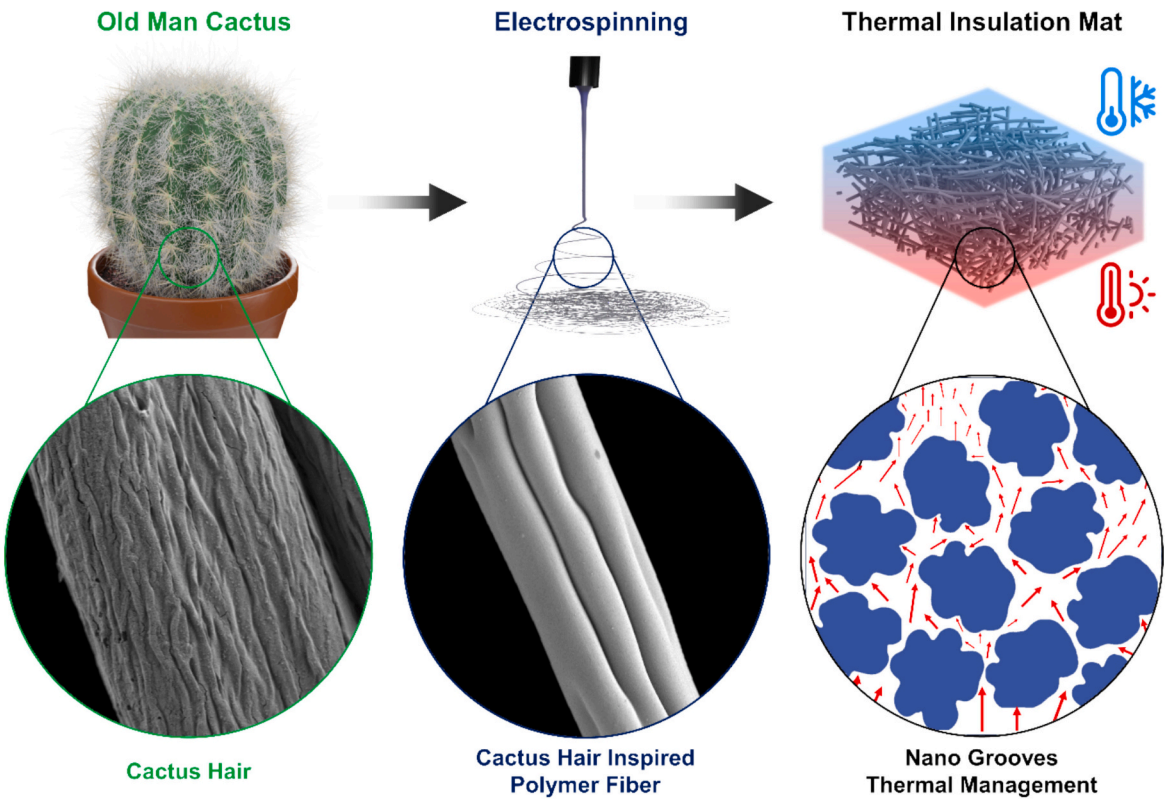

Fig. 1. Cactus hairs inspiration. Schematic diagram presenting the strategy for electrospinning bioinspired hair-inspired fibrous mats and their functional application as thermal insulation.

formation was added to supporting information (page S7 in SI). Individual fiber cross-section geometry investigations show a clear difference between sF and ngF. The circularity coefficient value (~0.87) and contour shape for sF were closer to a perfectly round shape (circularity coefficient = 1.00), whereas ngF has a much lower value (~0.64) (Fig. S3C).

One parameter used to express the differences in surface roughness of materials is the R_a - arithmetic average of profile height deviations from the mean line [35]. In the case of smooth fibers, the low value of the R_a (~20 nm), along with a slight deviation, suggests that the surface exhibits a lack of roughness, which is evident from the FIB-SEM images and the AFM roughness profile (Fig. 2A, C-E**).** For nanogroove fibers, there is an apparent increase in R_a to ~119 nm (Fig. 2B, C-E**).** Additionally, the depth of nanogrooves is close to the value presented by Guen et al., where surface roughness affects the heat conduction of material [31]. What is important is that the surface profile and roughness average of ngF and cactus hairs were similar (Fig. 2C, D**)**, demonstrating the biomimetic properties of our fibers. The nanogrooves on the fiber surface create nano roughness, which is crucial for obtaining thermally insulating materials and is explained further in this work.

2.3. Characterization of fibrous mats

The further characterization of two types of mats (nF and ngF) includes pore size, thickness, wettability, roughness, density, and specific surface area (BET), with all the details presented in the SI. The mean pore size values were 131.38 ± 119.48 μm for sF and 90.94 ± 73.96 μm for ngF, respectively (Fig. S4A, B). The thickness, water contact angle, and roughness of mats were similar and were ~410 μm, ~128°, and ~13 μm for both samples (Fig. S2C-F and Table S1). The density of samples varied, ~1.416 $g{\cdot}cm^{-3}$ for ngF and ~ 1.378 $g{\cdot}cm^{-3}$ for sF mats, and ~ 1.195 $g{\cdot}cm^{-3}$ for PC powder material. Specific surface area was ~22.177 $m^2{\cdot}g^{-1}$ for sF and ~ 1.357 $m^2{\cdot}g^{-1}$ for ngF (Table S1 and Fig. S5).

One of the main factors determining the properties of electrospun mats is the diameter and shape of the fibers [36]. For example, changing fiber diameter from micro to nanoscale or altering geometry from smooth shape to ribbon or groove results in reduced pore size and can affect mat thickness, wetting angle, and mechanical properties [37–40]. However, in this work, the average diameter of the sF and ngF fibers was similar. The only difference was in shape (see Fig. 2A, B), which did not affect pore size, thickness, wettability, roughness, and density of mats. The difference in specific surface area is caused by sample preparation (cutting) and the porous structure of sF. A more detailed discussion regarding specific surface areas can be found in SI, page S8.

2.4. Chemical analysis of mats

The Fourier Transform Infrared Spectroscopy (FTIR) spectra of mats indicating the specific peaks at 1161, 1188, and 1230 cm^{-1} for C—O bond stretching, 1386 cm^{-1} for C—H bending, 1500 and 1684 cm^{-1} for C═C stretching, and 1770 cm^{-1} related to C═O (Fig. 2F**)**. The glass transition temperature (T_g) of sF, ngF fibers, and PC granulate material (raw material) were evaluated using differential scanning calorimetry (DSC) and reached: 134.2 ± 1.0, 136.5 ± 1.3, and 152.7 ± 0.7 °C, respectively (Fig. 2G**)**. The average crystallinity of the electrospun fibers and PC granulate was found to be lower than 1 % for both samples. In addition, a DSC test was conducted from 25 to 80 °C for 30 cycles, which showed the thermal stability of sF and ngF (Fig. S6).

The chemical analysis showed no structural differences between samples with different individual-fiber geometries, confirming the amorphous structure [41]. Only the slight shift in T_g is caused by voids inside sF fibers [42]. The voids also caused differences in the density of fibers and specific surface area (Fig. S3). Nanogroove fibers (ngF) exhibited extensively lower gas sorption, reducing specific surface area. Contrary to expectations, this outcome is attributed to the sample

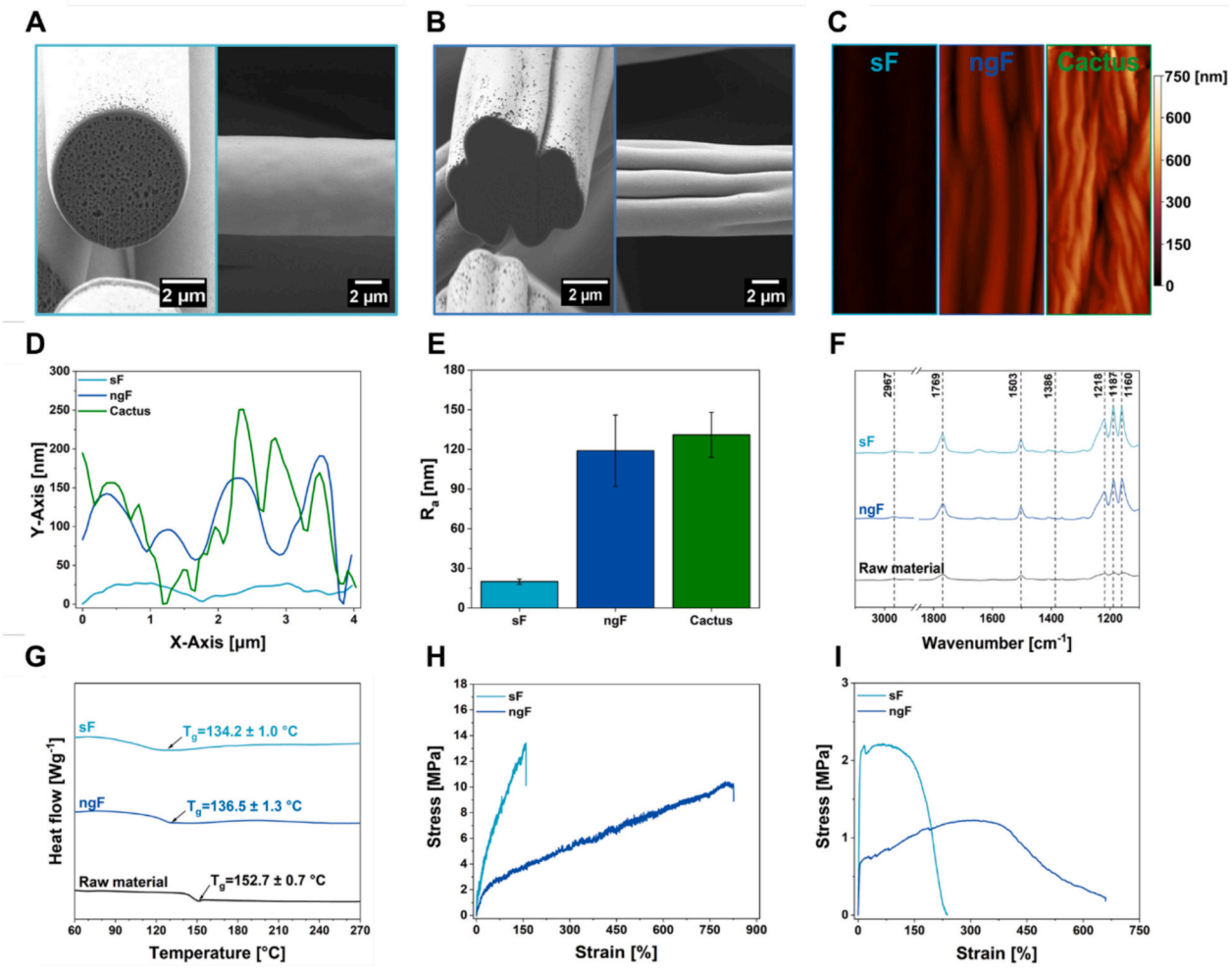

Fig. 2. Morphology, cross-section and surface investigation of single cactus hairs inspiration polymer fibers. (A, B) SEM micrographs showing surface morphology and cross-section of individual electrospun smooth (sF) and nanogroove (ngF) fiber. (C) AFM topography images of individual fibers - sF, ngF, and cactus hair indicating the differences in surface roughness. (D) Example of individual fiber sF and ngF surface profile used to calculate R_a from AFM images. (E) Bar graph of surface average roughness (R_a) for individual fibers sF and ngF, and cactus hair. (F, G) Representative DSC heating curves and FT-IR spectra for sF and ngF fibers, and PC granulate (raw material). (H, I) Representative stress-strain curve of sF and ngF individual fiber and fibrous mats.

preparation process (Fig. S5). Detailed discussion of gas adsorption results was explained in SI, see page S7–8.

2.5. Mechanical properties of individual fibers and mats

The mechanical properties of individual sF and ngF and mats were examined using a tensile module (Fig. 2H, I). Individual fibers were collected directly during electrospinning onto laser-cut rectangular paper frames with 1 × 2 mm openings. This enabled controlled isolation of straight, single fibers suitable for tensile testing using a 1 N force cell. The methodology is described in detail in the Materials and Methods. Individual smooth fibers exhibited ~1.83 and ~1.53 higher maximum stress (σ_{max}) and Young's modulus (E), but ~3 times lower strain at maximum stress (ε_{max}) and failure ($\varepsilon_{failure}$), and ~2.1 lower toughness (W) compared to those of individual nanogroove fibers. All results from mechanical testing and all stress-strain curves are summarized in the SI (Table S1 and Fig. S7). We observed a similar trend in the case of mats consisting of randomly oriented fibers, showing a higher σ_{max} and lower ε_{max}, $\varepsilon_{failure,}$ and W for sF mats than results for a ngF mat (Table S1).

In terms of the mechanical properties, we verified them for individual fibers and mats. The tensile test results demonstrate ~83 % and ~53 % higher tensile strength and Young's Modulus for sF but ~300 % lower strain and toughness than ngF. A similar tendency was previously observed for PVDF fibers, where smooth fibers exhibited higher tensile strength than grooved ones [43]. The higher tensile strength of sF is linked to the existence of voids inside fibers [44]. The presence of voids in the single fiber increases the packing of molecules in the structure [45]. making the chains less free to move and pull out, which increases the strength of the material while reducing elongation, as seen in sF [65]. The mats composed of ngF showed higher strain and toughness than sF based mat, which are desirable for thermal insulation applications (Fig. 2H, I; Fig. S7 and Table S1) [46]. In the randomly oriented fiber network, individual fiber strength significantly influences the mechanical properties of electrospun mats [47]. The random arrangement of fibers distributes stress and enhances mechanical performance due to interactions between the fibers, highlighting the significance of individual fiber stiffness [48].

2.6. Analysis of thermal properties

Starting with the thermal properties of individual fibers, we employed scanning thermal microscopy (SThM) to precisely map the heat transfer with a spatial thermal resolution (<50 nm) and remarkable thermal sensitivity (<0.01 °C), see Fig. 3A [49]. Previously, SThM was used to investigate the thermal conductivity of polyimide (PI) nanofibers, which was improved by adding silicon-nitride (SiN) particles

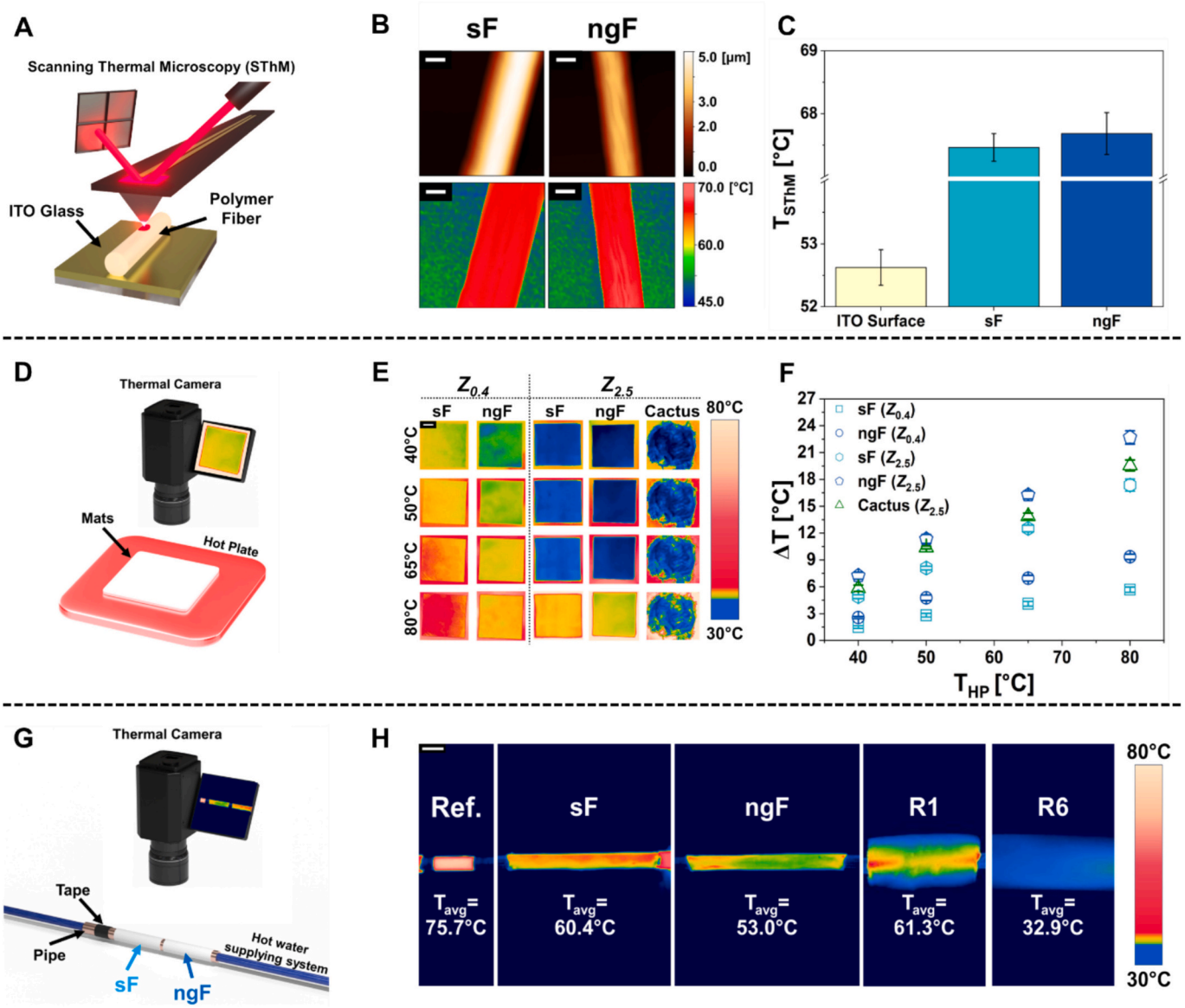

Fig. 3. Thermal insulation properties of polymer fibers and cactus hair mats. (A) Schematic of SThM experiment setup. (B) SThM representative scan maps (scale bar - 5 µm). (C) The average temperature measured by the SThM tip is presented in the bar graph. (D) Schematic of hot plate experiment setup to verify the performance of nanogroove fibers. (E) Thermal camera images of sF, ngF, and cactus hair mat measured at two different thicknesses (*Z*): 0.4 and 2.5 mm at hot plate set to 40, 50, 65, 80 °C (scale bar - 1 cm). (F) The graphs show the differences between the temperature (ΔT) of the reference sample (carbon tape) to sF and ngF mats for different hot plate temperature (T_{HP}). (G) Schematic of water piper experiment setup. (H) Comparison of thermal images of reference tape, sF, ngF electrospun mats and commercial rubber pipe insulation with 1 mm (R1) and 6 mm (R6) wall thickness mounted in hot water pipe system (scale bar - 1 cm).

[50]. The temperature recorded by the SThM reflects the rate of heat conduction when the probe contacts the sample's surface; a higher surface temperature of the tip indicates lower heat transfer between the tip and the sample, implying lower conductivity of the material. Therefore, SThM was used to investigate heat transfer in both types of fibers. Topographic and thermal images of individual sF and ngF showed similar tip temperature, at 67.46 ± 0.21 and 67.68 ± 0.33 °C, respectively (Fig. 3B, C).

The thermal insulation performance of the fibers and cactus hair mats was evaluated using a thermal camera, with measurements recorded at hot plate temperatures of 40, 50, 65, and 80 °C (Fig. 3D). For cactus hair mats, different thicknesses (Z) were achieved by trimming, resulting in 2.5, 5-, and 10-mm thicknesses (Fig. S8A). To compare it with polymer mats, greater *Z* values were achieved by stacking 1 to 5 layers of mats, reaching thicknesses from 0.4 cm ($Z_{0.4}$–1 layer) to 2.5 cm ($Z_{2.5}$–5 layers) (Fig. S8B, C). The thermal camera analysis showed a temperature difference (ΔT) between the hot plate and the samples (Fig. 3E, F and Fig. S9). Notably, a higher ΔT indicates greater thermal insulation properties of tested materials. For sF ($Z_{0.4}$), ΔT was approximately 1.5, 2.8, 4.1, and 5.6 °C at hot plate temperatures of 40, 50, 65, and 80 °C, respectively (Table S2). The ngF ($Z_{0.4}$) showed an approximately 65 % higher ΔT at all temperatures than sF samples, with values of ~2.5, 4.7, 7.0, and 9.4 °C, respectively. Higher ΔT for ngF mats was also observed across all tested thicknesses (Fig. S9 and Table S2). Interestingly, 2.5 mm thick ngF mats exhibited better thermal insulation performance than 2.5 mm thick cactus hair mats (Fig. 3E, F and Table S2). Layer stacking confirmed that, regardless of the insulation thickness, grooved fibers consistently exhibited better insulation properties. Furthermore, the proposed system has practical significance for the industry, enabling reduced production times, efficient material fabrication, and application in a layered form.

To further assess the mats' effectiveness in reducing heat loss, we

conducted an additional experiment involving a copper pipe to replicate a hot water circulation system in a building (Fig. 3G and **S10**). We directly deposited sF and ngF mats onto the copper pipe, which was connected to a continuously circulated hot water system. In buildings, water transported through pipes to heaters can reach approximately 80 °C during the cold season [5]. Thus, we selected this temperature for our experiment. In this work, the primary purpose of pipe insulation is to minimize heat loss from the pipe to the surrounding environment, addressing a critical issue in thermal insulation: Maintaining a stable temperature while reducing energy losses. The individual fiber diameter deposited on pipe was ~6 μm, and the thickness of the mat applied on pipe was ~110 μm for both types (Fig. S10B-D). For comparison, we used a commercial insulation rubber coating with wall thicknesses of 1 mm and 6 mm, named R1 and R6 (Fig. 3H), respectively. As a reference sample, we used a special tape (further details can be found in the materials and methods section), which resulted in a pipe surface temperature of ~75.7 °C. Importantly, the surface temperatures achieved with sF and ngF were ~ 60.4 and ~ 53.0 °C, respectively. For R1 and R6 insulation, surface temperatures were ~ 61.3 and 32.9 °C, respectively.

Lastly, we verified the thermal conductivity (λ) of fiber mats with a thickness of 2.5 cm ($Z_{2.5}$–5 layers). Changing the sample morphology from smooth to nanogrooved significantly affected the thermal conductivity of the tested materials, with values of ~42 for sF and ~ 36 $mW{\cdot}m^{-1}\ K^{-1}$ for ngF (Table S1). We conducted comparison of the thermal conductivity of the produced mats and the conventional materials used for pipe insulation (Fig. 4A). For example, the thermal conductivity of the rubber foam used for insulation in this work is ~35 $mW{\cdot}m^{-1}\ K^{-1}$, which is close to that of ngF, highlighting its potential for industrial applications. Additionally, the low thermal conductivity of the nanogrooved mats, combined with their lightweight and flexible structure, makes them promising candidates for use in energy-efficient thermal insulation systems, especially where space constraints or complex geometries are involved. To further assess the performance of our materials, we conducted a comparative analysis of thermal conductivity values reported for electrospun materials dedicated to thermal insulation applications over the last three years. In total, approximately 28 relevant publications were identified, reflecting a growing research interest in this area. As illustrated in Fig. 4B, the field shows a noticeable focus on composite systems, such as polymer fibers incorporating ceramic particles, as well as fully ceramic fibrous structures obtained through calcination or pyrolysis. There is significant interest in both composite and ceramic electrospun fibers due to their potential to offer enhanced thermal insulation performance; however, these materials often exhibit a wide range of thermal conductivity values. Moreover, their higher production costs and more complex fabrication processes reduce their feasibility for industrial-scale implementation compared to simpler polymer-based systems. For example, polyimide/polysulfone amide (PI/PSA) porous micro-nano fiber membranes demonstrated a thermal conductivity of ~45 $mW{\cdot}m^{-1}\ K^{-1}$, while hollow TiO_2 fibrous membranes achieved values around ~30 $mW{\cdot}m^{-1}\ K^{-1}$ [51,52]. These values are comparable to those obtained for our nanogrooved fiber mats, despite our use of a simpler and more scalable fabrication process.

We further demonstrated that modifying the geometry of individual fibers from smooth to a nanogroove surface improves the thermal insulation properties of the mat, resulting in a ~ 30 % decrease in sample surface temperature compared to a reference sample (~80 °C) for ngF with 2.5 cm ($Z_{2.5}$) thickness (Fig. 3E, F). It is important to note that ngF mats exhibit better insulation performance than natural cactus hair mats with the same thickness ($Z_{2.5}$). In hot water pipe experiment, despite the commercial rubber coating (R1) having an insulation thickness (~1.0 mm) ~10 times greater than ngF mats (~0.1 mm), ngF mats still resulted in ~9 °C lower surface temperature (~62 °C for R1 and ~ 53 °C for ngF). Furthermore, thermal measurements indicate that ngF mats possess similar or even better-insulating properties than commercial materials such as rockwool or rubber foam, confirming their potential for pipe insulation coatings (Fig. 4A). Moreover, low thickness and light weight of our coatings offer a major advantage for applications where insulation layer dimensions are critical, such as in the space industry [53].

When thermal flux flows through fibrous materials with high porosity, heat transfer behavior within these porous structures can be categorized into four components: solid and gas conduction, convection, and radiation [54]. Solid thermal conduction in porous materials is linked to phonon transport occurring at both solid/solid and solid/gas interfaces [55]. Reducing the pore size of fibrous materials weakens solid thermal conduction, which enhances the diffusion and specular scattering of phonons [56]. Additionally, fibers with small diameters create numerous tortuous channels within the materials. These channels serve as pathways for phonon scattering and trap more still air with low thermal conductivity, ultimately leading to a decrease in the effective thermal conductivity of the fibrous materials [57]. When fibrous materials have pores larger than 1 mm, thermal convection occurs due to heat flow within the porous structures. In contrast, when the pore size is smaller than 1 mm, thermal convection can be neglected because the small pore size limits the thermal transportation induced by gas flow. Radiative heat transfer is typically negligible at room temperature and standard pressure. However, this changes extensively for fibrous materials with nanofibers [57]. Reducing the fiber diameter to the nanoscale decreases the mean pore size. Consequently, due to their small pore size and high porosity, photon transport is suppressed, which can reduce radiative heat dissipation in fibrous materials [58].

From a material engineering point-of-view, especially for high-porosity 3D materials like aerogels, electrospun mats, foams, and sponges, insulating properties depend on solid- and gas-phase conduction [57,59–63]. Solid phase conduction in fibrous materials is strongly related to the type of material, geometry (type of fiber lattice), and fiber-

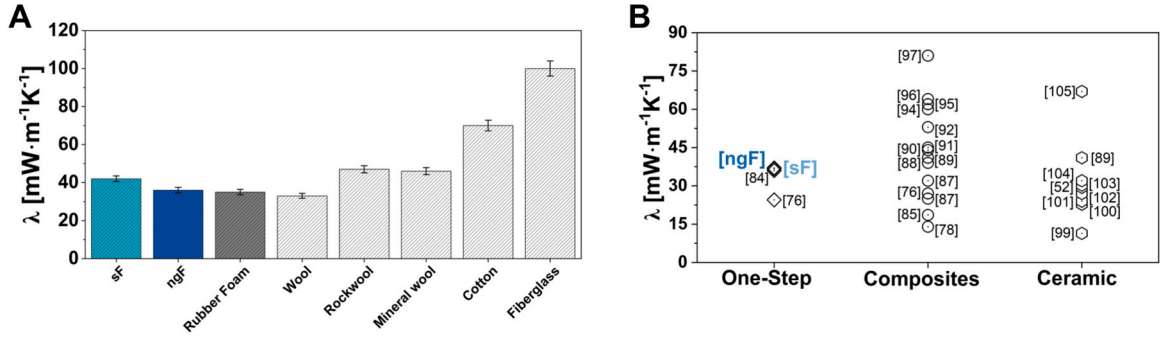

Fig. 4. Thermal conductivity comparison of commercial and electrospun materials. (A) Thermal conductivity values of electrospun fibers compared to commercial insulation pipe materials: rubber foam, wool, rockwool, mineral wool, cotton, fiberglass [76,82,83]. (B) Comparison of thermal conductivity values for different types of electrospun materials used as thermal insulation — one-step (produced by one-step electrospinning), composites (e.g., polymer fibers with ceramic particles), and ceramic composites (e.g., electrospun fibers subjected to calcination or pyrolysis) - based on data collected since 2021. [52,76,78,84–105]

to-fiber contacts [54]. Thermal properties of polymers depend on molecular chains, crystallinity, and molecular weight [64–66]. For example, aromatic structures in the polymer backbone, higher crystallinity, and molecular weight improve the thermal properties of polymers [65,67]. In the case of mat geometry, changing fiber diameter, thickness, and pore size affects the porosity of mats, thus, heat conduction [57,68]. Additionally, the contact points and adhesion between fibers are affecting the solid phase conduction of randomly oriented fibrous mats [69]. Merged fibers or a larger contact area between them can cause an increase in the number of so-called solid conduction pathways, thus affecting the insulating properties of the mats [68]. Notably, conduction in the gas phase related to the Knudsen number, which is based on the average free path of the gas at a given temperature and pressure, as well as the average pore size forming the void [68]. In the case of sF and ngF, the contact between fibers in the mats varies as the surface roughness is significantly higher for nanogroove fibers (Fig. 2C-I**)**. Additionally, their enhanced toughness and flexibility facilitate better contact with curved or irregular surfaces, minimizing conduction pathways and maintaining effective insulation [68]. Other characteristics, such as type of structure (amorphous), crystallinity, pore size, and porosity of mats, are similar. Moreover, although the average diameter of ngF fibers (5.17 ± 0.72 μm) is slightly smaller than that of sF fibers (6.35 ± 0.90 μm), the difference is not statistically significant. Thus, we rule out fiber diameter as a major factor in the thermal performance differences observed. Instead, our data clearly points to the role of surface nanogrooves as the dominant mechanism enhancing air trapping and reducing heat conduction in the ngF mats.

The thermal properties of polymers depend on the orientation of molecules, or crystallinity, which can influence the solid conduction mechanism in the material. However, for our two samples, these properties are similar [70]. Interestingly, despite the presence of pores in the sF, which can lead to lower thermal conductivity, there is still no visible difference in the thermal properties of the single fiber [71]. This is because the porosity within the single fiber is relatively very low (~11 %), and the pores are closed in the structure. In contrast, previous studies have shown that hollow double-shell fibers, with ~37 % of their structure being hollow, exhibit lower thermal conductivity compared to solid fibers [72].

The change in thermal conduction depends on gas-phase conduction, with air entrapped in mat structure by the nanogrooves of individual fibers, enhancing the thermal insulation. Radiative heat transfer and convection can be neglected due to the large fiber diameter (greater than 1 μm) and small mat pore size (less than 1 mm) [57,58]. The air molecules trapped in the mat between fibers reduce conduction through the air phase, a phenomenon known as the Knudsen effect (Fig. 5**)** [73]. The experimental work on the hot plate showed a straightforward difference in surface temperature between sF and ngF (Fig. 3E, F**)**. As the temperature rises, the heat flow also increases. Still, heat flow is reduced because more air is enclosed in the nanogrooves of fibers and between the fibers in mats [74]. Thus, ngF mat's surface reaches a lower temperature than the sF (Fig. 3E, F**)** [75]. In assessing thermal conductivity, our objective is to quantify the transfer of heat facilitated by thermal conduction. In the mats, the predominant medium is gaseous (air), thereby dictating the dominance of gas-phase thermal conduction. Consequently, we discovered the impact of fiber morphology (smooth and nanogroove) on the thermal conductivity values, thus on solid-phase conduction, and proved a gas conduction effect (hot plate and hot pipe experiment). Although smooth fibers (sF) exhibited ~11 % internal porosity due to phase separation under high humidity conditions, FIB-SEM analysis revealed that nanogroove fibers (ngF) had a solid internal structure. While such pores can theoretically reduce solid-phase thermal conductivity by disrupting phonon transport, our results suggest that surface morphology, specifically nanogrooves, have a greater impact. The enhanced insulation of ngF mats arises primarily from air entrapment on the fiber surface and between fibers, dominating over minor effects of closed internal voids in sF. This highlights that nanoscale surface architecture plays a more decisive role in gas-phase thermal resistance than moderate internal porosity in the polymer matrix. Wang et al. tested the thermal insulation properties of grooved PS fiber geometry. However, they did not address the mechanism behind the mats' insulating effects [76]. Additionally, Paul and Diller showed similar results, where grooved fibers exhibited better thermal insulation performance than smooth fibers [77]. In addition, a more developed (grooved) structure of fibers leads to a reduction in thermal conductivity. However, the authors used polyester, a semicrystalline material, and did not verify the thermal properties of a single fiber. In another work, thermal insulation properties of electrospun mats were enhanced due to the use of core-shell hollow fibers and nanopores on the fibers' surface [78]. Nonetheless, other studies show that changing the surface roughness at the nanoscale can drastically affect the heat flow across the material's surface, leading to a change in insulating properties, which we observe for ngF mats [31,32,79]. Noto et al. presented results where even small changes in geometry can reduce heat motion, which is consistent with our results [80]. Further, it was proved by numerical simulation, where open nanovoids (like nanogrooves) on the surface reduce the effective thermal conductivity of porous structures like electrospun mats [71]. Molecular simulation studies of entrapped molecules in material nanoscale grooved surfaces showed expanded heat

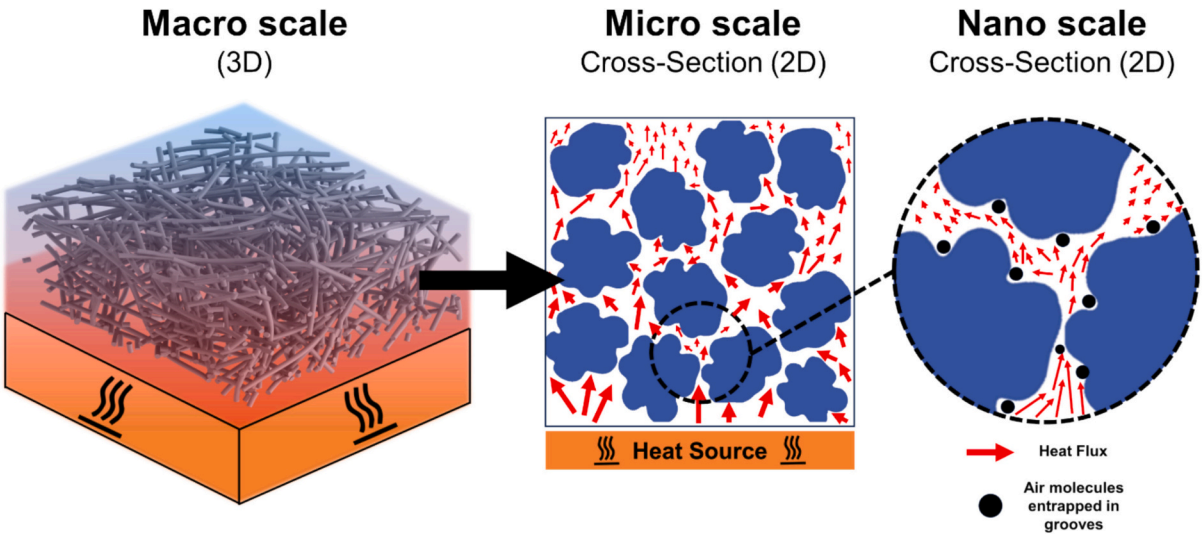

Fig. 5. Nanogrooves effect. Schematic explanation of nanogrooves effect on heat flow behavior through ngF mats.

transfer [81]. The grooved scales exhibited different patterns of molecular packing, leading to changes in heat transfer properties, which correlate with our results.

2.7. Numerical simulation of heat flow through smooth and nanogroove fibers

To verify further the effect of nanogrooves on the thermal insulation properties of mats, we performed a numerical 2D heat transfer simulation through 1, 2, 5, and 10 smooth and nanogroove fibers in a defined arrangement (Fig. S11). Simulations indicate the relation between the temperature at the fibers' surface (T_{sim}) and the difference between sF and ngF temperatures (ΔT_{sim}) concerning the number of fibers in the random arrangements (Fig. 5A). For sF, T_{sim} was 79.62, 79.47, 79.37, and 79.05 °C, and for ngF it was 79.63, 79.45, 79.33, and 78.97 °C for simulations with 1, 2, 5, and 10 fibers, respectively.

In the case of a numerical simulation of heat flow through a single fiber, the difference between the materials is not remarkable, which correlates with SThM results (Fig. 2B, C). In the context of our work, it is evident that gas-phase conduction is less important than solid-phase conduction for a single fiber. However, as the number of fibers in the system increases, the temperature difference between sF and ngF rises (Fig. 5A). Thus, gas-phase conduction has visible effects, confirming the surface roughness consequences for thermal insulation, as demonstrated by thermal camera results for mats (Fig. 3E, F). Similar results for heat transport simulations of rough surfaces were demonstrated for heat sinks and tubes, verifying the effect of surface roughness [106–108].

2.8. Energy saving analysis of porous thermal insulation coatings

Given the demand for energy-saving technologies and new directives related to the reduction of polymer waste, fundamental economic analysis of the mass-produced polymer in terms of energy savings and recyclability was undertaken. The measurements were based on the hot water pipe insulation test data (Fig. 3H). In addition, we calculated the energy saved per unit area (P_A) and per 1 g of insulation material mass (P_M) for R1, R6, sF, and ngF, which was around 11.9, 18.6, 16.4, 23.2 $kW{\cdot}m^{-2}$, and 0.06, 0.04, 0.08 and 1.17 $W{\cdot}g^{-1}$, respectively (Fig. 6B and Table S3).

The energy-saving showcase demonstrates enormous potential for reducing energy consumption. Specifically, insulation type R1 achieved a 32 % reduction in heat loss, with energy savings of 27.1 W. In contrast, insulation type R6 outperformed others by delivering a remarkable 74.4 W of energy savings, representing an 88 % reduction in heat loss compared to bare pipe (Table S3). The ngF and sF insulation types also demonstrated significant energy savings, with the reduction of 31.2 W (52 %) and 16.4 W (37 %), respectively. Furthermore, when considering energy savings per unit area (P_A), ngF exhibited the highest value at 23.2 $kW{\cdot}m^{-2}$ and excelled in terms of energy savings per gram of material mass (P_M) with a value of 1.17 $W{\cdot}g^{-1}$ (Fig. 6B). Parameters such as the amount of material used, the energy saved by the system per area (P_A), and per mass (P_M), show a potential perspective in using nanogroove fiber mats as an insulating material. R6, despite having the highest energy saving (~74.4 W), generates the highest amount of waste (2000 g), which is 52 times more than fiber mats (~38 g for sF and ngF) (Table S3). Importantly, comparing the energy retained per unit area and mass of insulation used, ngF mats showed 25 % more P_A and ~ 30 times more P_M than R6, (Fig. 6B). From the environmental perspective, the commercial rubber coating (R1, R6) is a hard-to-recycle or non-recyclable material [109]. In contrast, the PC used to produce mats belongs to the category of fully recyclable materials, which is desirable in achieving a sustainable future for thermal insulation [110,111].

3. Conclusion

The novel approach in our studies led to the development of recyclable polymer mats as an alternative to the current thermal insulations. We successfully created thermally insulating mats based on the nanogrooved fibers, having 65 % higher ΔT for all temperatures than fibers without nanogrooves. This proves that biomimicking nanogroove structures from cactus hair helps us to develop universally applicable, flexible, mechanically robust, thermally insulating fibrous mats. All of these can be easily fabricated using single-step electrospinning under controlled-humidity. Our study clearly demonstrates that the thermal insulation properties of these materials are significantly influenced by the roughness and morphology of the individual fibers in the mats. Importantly, we verified the performance of individual fibers using scanning thermal microscopy, which was theoretically confirmed via numerical simulation. The random arrangements of fibers in mats and coatings enhance thermal insulation by capturing air in the nanogrooves of the electrospun nonwoven fibers. Inspired by the Old Man Cactus hair mats, nanogrooved fibers (ngF) achieved ~30 % higher efficiency in the thermal insulation of water pipes compared to smooth fiber (sF), and ~ 10 % higher than commercial rubber coating under identical experimental conditions. Apart from excellent thermal insulation, the mats showed outstanding mechanical performance, with an exceptional boost

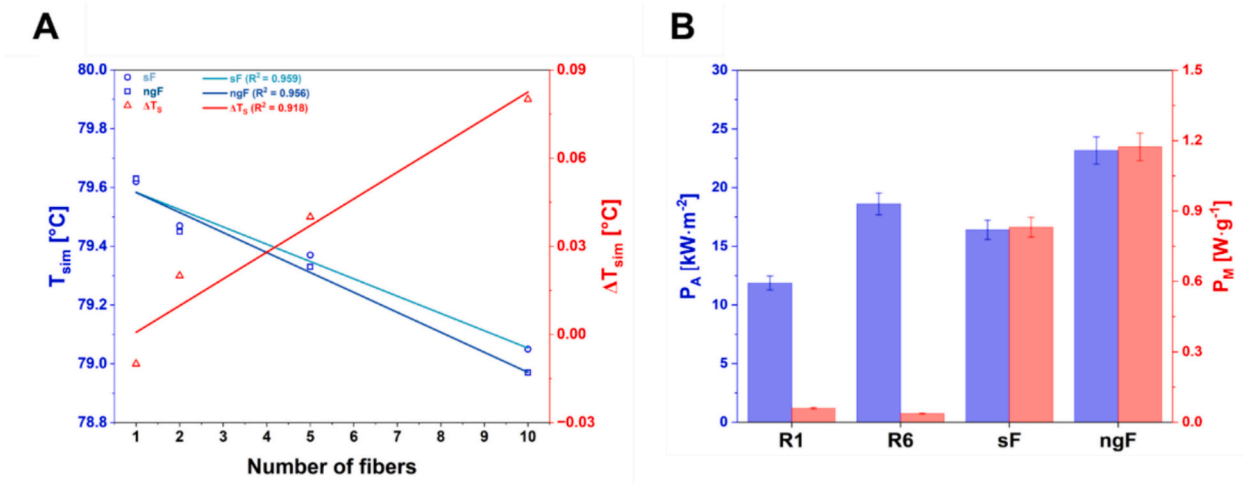

Fig. 6. Heat transfer simulation and energy saving analysis of cactus hair inspired fibers. (A) Relation between fiber surface temperature (T_{sim}) and the difference between sF and ngF temperatures (ΔT_{sim}) to the number of fibers used in the simulation. (B) Results of energy saved per unit area (P_A) and per 1 g of insulation material mass (P_M) for commercially used materials (R1 and R6) and both types of PC mats.

in the toughness and strain of ngF mats. Compared to commercial insulation, nanogroove fibrous coatings demonstrate 25 % higher energy savings per unit area and ~ 29 times higher energy savings per gram of material mass. In summary, we have demonstrated a practical and straightforward one-step strategy for increasing the applicability and effectiveness of bioinspired nanogroove fibrous mats as thermal insulation.

4. Materials and methods

4.1. Materials

Old Man Cactus (*Cephalocereus senilis*) was brought from the local plant shop and kept in laboratory ambient conditions (21–23 °C and 30–40 % RH). The hairs were carefully extracted from the plant by manually trimming them. The thickness of the hair layer was measured using a ruler after extraction of areole perpendicular to the cactus skin. To produce polymer fibers, 24 wt% polymer solution of polycarbonate granulate (PC, M_w = 29,800 g·mol^{-1}, Makrolon 3108, Goodfellow GmbH, Germany) granulate was dissolved in a mixture of dimethylacetamide (DMAc, Sigma Aldrich, UK) and tetrahydrofuran (THF, Sigma Aldrich, UK) at 1:1 weight ratio. The solution was stirred at 700 rpm for 2.5 h on a hot plate set at 60 °C (RCT basic, IKA, Germany). The mass of the samples was measured using a high-precision analytical balance (XPR, Mettler Toledo, Switzerland).

4.2. Fabrication of cactus hair inspired fibers

Cactus hair-inspired fibers were produced via electrospinning (EF300, SKE Research Equipment, Italy) at $T = 22 \pm 1$ °C and RH = 30 ± 1 % for nanogroove fibers and 60 ± 1 % for smooth fibers. Preliminary trials were conducted at various relative humidity (RH) levels including 20 %, 40 %, 50 %, and 70 %. However, these conditions led to process instabilities such as needle clogging, jet interruptions, and uneven fiber deposition. To ensure consistent and reproducible mat fabrication suitable for further testing, electrospinning was limited to stable RH conditions of 30 % and 60 %. A voltage of 31 kV was applied to the needle (0.51 mm inner and 0.82 mm outer diameter - 21G x 1 1/2″) kept at 27 cm from the grounded rotating stainless-steel drum with 20 cm diameter at 1200 rpm that was used as a collector to deposit individual fibers and 20 rpm formats. The flow rate was set to 3.9 ml·h^{-1}. Electrospinning time was 1 s for individual fibers and 90 min for further tested mats. The samples were deposited directly on baking paper for all analysis and laser-cut paper frames for mechanical testing. For the hot water pipe test, fibers were deposited directly on a 6 mm diameter copper pipe rotating at 20 rpm for 15 min, keeping the same parameter as above.

4.3. Surface morphology and 3D tomography

Morphology and cross-section investigation of fibers and Old Man Cactus hair and bundle diameter were carried out using scanning electron microscopy (SEM, Merlin Gemini II, ZEISS, Germany) at 2.5 kV accelerating voltage, 105 pA current and 4–9 mm working distance. Prior to the SEM analysis, samples were coated with an 8 nm thick Au layer using a sputter coater (Q150RS, Quorum Technologies Ltd., UK). Cross-section imaging of fibers was achieved using a freeze-fracture method where samples were immersed in liquid N_2 for 10 min and cracked using a scalpel prior to SEM imaging.

3D tomography of the fibers was achieved with FIB-SEM (Neon CrossBeam 350, Zeiss, Germany), using the Ga + ion beam at a current of 50 pA and voltage of 30 kV. SEM images of the cross-sectioned samples were taken at a current of 500 pA and voltage of 3 kV. The 3D reconstructions were prepared using Avizo v8.1 software. The circularity of fibers, mats pore fraction, and size were calculated based on SEM and FIB-SEM images using the analyze particles function in ImageJ software (version 1.51, Fiji, USA). The average thickness of the mats was measured using a light microscope (Axio Imager M1m, ZEISS, Germany) imaging in the z-direction from 10 different points on the samples.

4.4. Roughness of individual fibers and mats

An atomic force microscope (AFM, CoreAFM, Nanosurf) was used to measure the surfaces of fiber samples and cactus hair. Areas of 4 × 10 μm for each sample were obtained with Dynamic Force Mode (Tapping Mode) using HQ:NSC18/Al (μMasch, Bulgaria) probes. All measurements were carried out with a scan rate of 1 Hz. Data processing was carried out using Gwyddion open-source software (version 2.62). R_a is the arithmetic mean of the absolute values of the surface departures from the mean plane, which describes the roughness of the measured area. The average R_a values were calculated based on 3 different measurements performed on one sample representative for each material. A profilometry study was conducted using an optical profiler (Veeco, WykoNT9300, USA) at the following settings: objective (20×), field-of-view multiplier (0.55×), and sampling area (910 nm) to obtain the roughness average (R_a) of mats. Density and specific surface area analysis.

Density measurements were conducted using a helium pycnometer (Anton Paar, Ultrapyc 5000 Micro), calibrated with standard reference material to ensure accuracy and precision. Approximately 600 mg of each prepared sample was weighed and placed in the sample chamber, which was then sealed and purged with high-purity helium gas. The helium gas filled the space around the sample, and the pressure was measured to calculate the volume of the sample chamber. This process was repeated 20 times for consistency and low % variance. The density of each sample was calculated based on the mass and the measured volume, with results averaging at least 15 independent measurements to ensure reproducibility and accuracy.

The Brunauer-Emmett-Teller (BET) surface area analysis was performed using a gas sorption analyzer (NOVA 800, Anton Paar, USA) to quantify changes in specific surface area (surface area per mass of fibers) between the two fiber types. Specific surface area was measured using nitrogen gas physisorption at 77 K. Samples were divided into smaller pieces and placed as beads into a 9 mm diameter measuring cell using a filling rod. This division was done to prevent excessive compaction of the material, which could affect its texture and, consequently, the BET surface area. Before the surface area characterization, the fibers were degassed in a vacuum oven at 105 °C for 24 h. Full adsorption and desorption isotherms in the relative pressure range of 10^{-4} to 0.99 p/p_0 were recorded. Relative pressures ranging from 0.05 to 0.30 were used to calculate the surface area via BET using Kaomi for Nova software (Version 2023). The specific surface area of each fiber type was analyzed in duplicate ($N = 2$). Each replicate included approximately 600 mg of electrospun fibers fabricated from a single electrospinning solution. The ex-situ SEM imaging of the fibers after gas adsorption analysis was used to ensure that there was no considerable difference in texture after degassing in 105 °C.

Microporosity measurements were conducted using the gas adsorption analyzers (ASAP 2020, Micromeritics Instrument Corp., USA). The system was calibrated with high-purity reference materials to ensure accuracy and reproducibility. Approximately 600 mg of each pre-treated sample (the same as for N_2 adsorption) was used. The CO_2 adsorption isotherms were measured at 273 K using high-purity (99.999 %) CO_2 gas. The adsorption measurements were conducted in a pressure range from 0.001 to 0.03 p/p0.

4.5. Wetting properties

The static contact angles on mats, deposited on glass slides, were measured using deionized (DI) water (pH ~ 5, surface tension $\gamma = 72.2$ mJ·m^{-2}, Spring 5UV purification system – Hydrolab, Poland). The images of droplets were captured using a DSLR camera (EOS 700D, lens EF-

S 60 mm f/2.8 Macro USM, Canon, Japan) ten seconds after the deposition of 3 µl droplets on the samples. The experiments were conducted at 25 ± 1 °C and RH of 45 ± 1 %. Contact angles were determined for 10 different droplets deposited on the fibers using ImageJ's drop shape analysis plugin (version 1.51, Fiji, USA).

4.6. Chemical characterization

Thermal analysis was performed with differential scanning calorimetry (DSC 3, Mettler Toledo, Switzerland) at a heating rate of 10 K·min^{-1} from −25 to 300 and from 25 to 80 °C for thermal stability test (30 cycles). For statistics, three samples of fibrous mats and PC granulate were examined. Presented values are averaged from 3 independent tests. The molecular structure of was investigated with Fourier Transform Infrared Spectroscopy (FTIR, Nicolet iS5, Thermo Fisher Scientific, USA). Obtained fibers prepared 24 h prior the tests were compared to unprocessed powder. For each sample, 32 scans with a resolution of 4 cm^{-1} in the 400–4000 cm^{-1} range were performed.

4.7. Mechanical testing

The electrospun fibers were deposited directly on the surface of laser-cut rectangular paper frames with hole of 1 × 2 mm for individual fibers and 20 × 8 mm for mats, which were later tested in a tensile machine (1 N cell for individual fibers and 20 N for mats, Kammrath & Weiss, Germany) at $T = 24 \pm 1$ °C and RH = 50 ± 1 %. The extension rate was 1 µm·s^{-1} for individual fibers and 20 µms^{-1} for mats.

The stress was calculated using a force measured by the tensile module divided by a sample cross-section area (A_{cs}). For individual fibers, the cross-section area was defined as a circle ($A_{csF} = \pi \cdot R$), where R is taken as the average diameter of the fibers (D_f). For mats, the stress was calculated as force divided by the cross-section area of mats - the average thickness to width (8 mm) of the mat. Young's modulus of individual fibers was calculated based on linear fitting in 0.5 to 1 % strain region. The average values for maximum stress (σ_{max}), strain at maximum stress (ε_{max}), strain at failure ($\varepsilon_{failure}$), Young's Modulus (E), and toughness (W) were calculated from 5 separate measurements using the integrate function in OriginPro software.

4.8. Thermal conduction measurements of individual fibers

The thermal conduction behavior of individual sF and ngF was examined using an atomic force microscope (AFM) equipped with a scanning thermal microscopy (SThM) module (CoreAFM by Nanosurf, Switzerland, and VertiSenseTM by AppNano, USA, respectively). The measurement method was based on a previous report [50]. A VTP-375 thermal probe containing a Si cantilever with a hollow silicon dioxide tip (k = 0.9 N·m^{-1}) integrated with a 50 nm thermocouple at the tip's apex was utilized for the measurements. The cantilever tip was heated to a stable temperature of approximately 80 °C using the AFM laser. We selected three randomly deposited fibers for each sample to obtain accurate measurements and simultaneously gathered topography and thermal data over a 30 × 30 µm scan area. We took measurements at a minimum of 3 distinct locations on each sample. All SThM measurements were carried out using the same probe to ensure consistency and eliminate any thermal transport variations related to the probe. To ensure consistent heat transfer between the tip and the scanned surface, the scan speed was set to 3 s per line. To avoid any erroneous reading resulting from the circular shape of the fibers, we only considered values from the apex of the fibers when calculating the average temperature for each sample. Measurements were conducted in a single session using the same SThM probe to maintain consistent heat transport and room conditions. The ambient conditions in the room during the experiments were at RH = 47 ± 1 % and $T = 24 \pm 1$ °C. The data obtained from the experiments were processed using Gwyddion (v2.56, Gwyddion.net) and OrginPro (2022 SR1, OriginLab, USA) software.

4.9. Thermal insulation and thermal conductivity tests of mats

Two experiments verified the insulating characteristics of the mats. In the first, all the fibrous mats were cut into a square (4 × 4 cm) using the laser cutter and then placed on a hotplate (TLC plate heater III, CAMAG, Switzerland). For the test, mats were stacked into 1–5 layers (0.4 mm - 2.5 mm thickness) and pressed with 0.5 kg steel weight for 3 h to minimize the influence of interlayer air. The plate was heated to a specific temperature: 40, 50, 65, and 80 °C, and then mats were placed on a hot plate for 30 min to stabilize the temperature. In addition, a vinyl electrical tape (Scotch Super 33+, 3 M, USA) with a constant emissivity of 0.96 was placed on the hot plate as a reference. The distance between the thermal camera and the heating plate was 50 cm. Next, fibrous mats were analyzed using a thermal camera (T560, FLIR, USA). To ensure a precise measurement, the camera was calibrated based on material with known emissivity (vinyl electrical tape - 0.96) and performed in stable environment conditions ($T = 23 \pm 1$ °C and RH = 41 ± 1 %) according to the camera manufacturer instructions. The average surface temperatures were calculated using the average square in FLIR Tools software from 5 separate measurements.

A hot water pipe experiment was conducted to verify the applicability of the manufactured mats as thermal insulation coatings (Fig. S10). A vinyl electrical tape and mats were placed on the Cu pipe with 6 mm outer diameter (OD), 4 mm inner diameter (ID), and 1 mm wall thickness (Fig. S10). Rubber pipe insulation (6 mm ID, 6 mm wall thickness, K-flex ST, Poland) was used to compare commercial material to produced mats. Additionally, to reach the manufactured mats more easily with commercially used insulation, a 5 mm thickness was cut out from the previously mentioned material to get 1 mm thick rubber insulation. Then, hot water with a temperature of 80.0 ± 0.5 °C was pumped into the system using a water pump with 9 l·min^{-1} water flow rate. During the entire test, the water temperature was monitored using a thermocouple (SE000 Type K, Pico Technology, UK) connected to a USB data logger (TC08, Pico Technology, UK) to confirm the stability of the water temperature. The temperature of the mats was verified using the same thermal camera as above. Both experiments were performed in a room with stable conditions, where the temperature and humidity were 24 ± 1 °C and 50 ± 1 %, respectively.

The thermal conductivity of mats was determined with a thermal analyzer (Trident TCi, C-Therm Technologies Ltd., Canada) equipped with Modified Transient Plane Source (MTPS) method following ASTM D7984–16 measurement protocol, carried out under stable room conditions ($T = 22 \pm 1$ °C and RH = 40 ± 5 %). The calibration of machine was performed for textile materials (C-Therm Technologies Ltd., Canada). For the test, mats were cut into 90 mm discs, stacked into 5 layers (2.5 mm thickness) and pressed with a 0.5 kg steel weight.

4.10. Heat transfer simulation of individual fibers

The heat transfer simulation, considering air temperature rise from thermal buoyancy forces and conductive heat transfer through fibers, was conducted using COMSOL Multiphysics (version 5.6, COMSOL Inc., Sweden). 2D steady-state models were used, assuming a high length-to-diameter ratio of the fibers. The geometry was based on FIB-SEM images (Fig. S3A, B). The arrangement of fibers in the simulation (for 4 fibers) was determined by cutting several fibers using FIB (Fig. S12). Additionally, nanogroove fibers were randomly rotated from the center point. Incorporating material information such as thermal conductivity of polycarbonate and surface emissivity (0.85) of the fibers. For the heat transfer in solids and fluids, PC was used as the solid, and air was used as the medium for the internal pores and the fluid around the fibers. The set temperature for all cases was 353.15 K set to the bottom boundary. The top of the fluid domain was set as an open boundary at 293.15 K. The laminar flow interface was used with no slip conditions on all surface boundaries of the fibers. A normal inflow velocity of 0.01 m/s and a constant gravity constant was used. The outlet and open boundary

conditions were used for the top fluid boundary conditions.

4.11. Economic analysis of thermal insulation mats

The economic insulation for a copper pipe was calculated with the following various parameters to optimize energy efficiency and reduce costs in a fluid flow system (Table S4). The dimensions included the length of the pipe (L) - 100 m, the outer diameter of the bare pipe (d) - 0.006 m, and the surface area of the pipe (A). Temperature considerations involved the ambient temperature (T_a) of 298.15 K, the pipe wall temperature (T_h), and the insulation thickness (t). The thickness and total mass of the insulating material are important factors for optimizing insulation energy savings. The internal heat transfer coefficient is influenced by the flow rate ($Kg{\cdot}sec^{-1}$) set to 0.1505, and internal diameter (d_i) of the pipe, 0.004 m, and the fluid temperature (K) of 353 K. Thermal properties such as the thermal conductivity of copper (K_{Cu}) 401 $W{\cdot}m^{-1}{\cdot}K^{-1}$, thermal conductivity of air (K_{Air}) 0.024 $W{\cdot}m^{-1}{\cdot}K^{-1}$, and surface heat transfer coefficient ($h_{conv,ext}$) was used to calculated the total heat losses. The mass of the samples was measured by analytical balance (XPR105DR, Mettler Toledo, Switzerland).

To establish the surface heat transfer coefficient $h_{conv,ext}$, the Rayleigh number ($R_{ray.}$) was employed. The Rayleigh number was calculated using the following formula.

$$R_{ray.} = \frac{\left(g \times \beta \times (T_h - T_a) \times d^3\right)}{(\mu \times \alpha)}, \quad (1)$$

where g is the acceleration due to gravity, β is the thermal expansion coefficient, μ is the dynamic viscosity of the fluid, and α is the thermal diffusivity of the fluid.

The surface heat transfer coefficient was calculated with the following equation [112].

$$h_{conv,ext} = \frac{K_{Air} \times 0.125 \times Ra_d^{0.333}}{d}, \quad (2)$$

The calculation of total heat loss (Q) from the surfaces was determined using the equation.

$$Q = h_{conv,ext} \times A \times (T_h - T_a), \quad (3)$$

Additionally, the total heat loss from the bare pipe (Q') was calculated using a similar approach. The Power Saved (P) was then derived by the following equation.

$$P = Q - Q', \quad (4)$$

4.12. Statistical analyses

The statistical analysis was performed using Student's t-test with OrginPro (2024 SR1, OriginLab, USA) software. For all tests, the significance was set at $p < 0.05$. Data are expressed as the arithmetic average ± standard deviation (SD).

CRediT authorship contribution statement

Daniel P. Ura: Writing – review & editing, Writing – original draft, Visualization, Validation, Methodology, Investigation, Formal analysis, Data curation, Conceptualization. **Piotr K. Szewczyk:** Writing – review & editing, Visualization, Investigation. **Gregory Parisi:** Writing – review & editing, Visualization, Software, Investigation. **Andrzej Osak:** Writing – review & editing, Methodology, Investigation. **Bartosz Puzio:** Writing – review & editing, Methodology, Investigation. **Jan Wrona:** Writing – review & editing, Investigation. **Il-Doo Kim:** Writing – review & editing, Writing – original draft, Visualization, Conceptualization. **Urszula Stachewicz:** Writing – review & editing, Writing – original draft, Supervision, Resources, Methodology, Funding acquisition, Conceptualization.

Funding

Horizon 2020, ERC grant agreement no. 948840.

Declaration of competing interest

The authors declare that they have no known competing financial interests or personal relationships that could have appeared to influence the work reported in this paper.

Acknowledgments

This study was conducted as part of the BioCom4SavEn project funded by the European Research Council under the European Union's Horizon 2020 Framework Programme for Research and Innovation (ERC grant agreement no. 948840). Research project supported partly by the program "Excellence initiative – research university" for the AGH University of Krakow in Poland.

D. P. U and P. K. S acknowledge the financial support by the Foundation for Polish Science (FNP), fellowship (START 090.2023 and START 080.2023). The authors acknowledge Joanna Knapczyk-Korczak for cactus hair samples.

Appendix A. Supplementary data

Supplementary data to this article can be found online at https://doi.org/10.1016/j.cej.2025.166441.

Data availability

The data that support the findings are available as the Supporting Information of this study and/or are available from the corresponding author upon reasonable request.

References

[1] M. Farghali, A.I. Osman, I.M.A. Mohamed, Z. Chen, L. Chen, I. Ihara, P.S. Yap, D. W. Rooney, Strategies to save energy in the context of the energy crisis: a review, Environ. Chem. Lett. 21 (4) (2023) 2003–2039, https://doi.org/10.1007/s10311-023-01591-5.

[2] A. Ahmed, T. Ge, J. Peng, W.C. Yan, B.T. Tee, S. You, Assessment of the renewable energy generation towards net-zero energy buildings: a review, Energ. Build. (2022) 256, https://doi.org/10.1016/j.enbuild.2021.111755.

[3] D. Wang, Heat loss along the pipeline and its control measures, SN Appl. Sci. 5 (1) (2023), https://doi.org/10.1007/s42452-022-05226-2.

[4] M. Kayfeci, Determination of energy saving and optimum insulation thicknesses of the heating piping systems for different insulation materials, Energ. Build. 69 (2014) 278–284, https://doi.org/10.1016/j.enbuild.2013.11.017.

[5] M. De Rosa, V. Bianco, Optimal insulation layer for heated water pipes under technical, economic and carbon emission constraints, Energy (2023) 270, https://doi.org/10.1016/j.energy.2023.126961.

[6] A. Keebaş, M. Ali Alkan, M. Bayhan, Thermo-economic analysis of pipe insulation for district heating piping systems, Appl. Therm. Eng. 31 (2011) 3929–3937, https://doi.org/10.1016/j.applthermaleng.2011.07.042.

[7] A. Nana, R. Cyriaque Kaze, T. Salman Alomayri, H. Suliman Assaedi, J. G. Nemaleu Deutou, J. Ngouné, H. Kouamo Tchakouté, E. Kamseu, C. Leonelli, Innovative porous ceramic matrices from Inorganic Polymer Composites (IPCs): microstructure and mechanical properties, Constr. Build. Mater. (2021) 273, https://doi.org/10.1016/j.conbuildmat.2020.122032.

[8] M. Rafiq, M. Shafique, A. Azam, M. Ateeq, The impacts of nanotechnology on the improvement of liquid insulation of transformers: emerging trends and challenges, J. Mol. Liq. 302 (2020), https://doi.org/10.1016/j.molliq.2020.112482.

[9] J.E. Contreras, E.A. Rodríguez, Nanostructured insulators – a review of nanotechnology concepts for outdoor ceramic insulators, Ceram. Int. 43 (12) (2017) 8545–8550, https://doi.org/10.1016/j.ceramint.2017.04.105.

[10] N.K. Katiyar, G. Goel, S. Hawi, S. Goel, Nature-inspired materials: emerging trends and prospects, NPG Asia Mater. 13 (1) (2021), https://doi.org/10.1038/s41427-021-00322-y.

[11] S. Metwally, S. Martínez Comesaña, M. Zarzyka, P.K. Szewczyk, J. E. Karbowniczek, U. Stachewicz, Thermal insulation design bioinspired by microstructure study of penguin feather and polar bear hair, Acta Biomater. 91 (2019) 270–283, https://doi.org/10.1016/j.actbio.2019.04.031.

[12] C. Zhang, D.A. McAdams, J.C. Grunlan, Nano/micro-manufacturing of bioinspired materials: a review of methods to mimic natural structures, Adv. Mater. 28 (30) (2016) 6292–6321, https://doi.org/10.1002/adma.201505555.

[13] J.E. Keeley, S.C. Keeley, Crassulacean Acid Metabolism (CAM) in high elevation tropical cactus, Plant Cell Environ. 331 (12) (1989) 336, https://doi.org/10.1111/j.1365-3040.1989.tb01948.x.

[14] L. Kundanati, N.G. Di Novo, G. Greco, S. Siboni, C. Della Volpe, A. Bagolini, N. M. Pugno, Multifunctional roles of hairs and spines in old man of the andes cactus: droplet distant coalescence and mechanical strength, Phys. Fluids 34 (1) (2022), https://doi.org/10.1063/5.0066153.

[15] J.D. Mauseth, Structure-function relationships in highly modified shoots of Cactaceae, Ann. Bot. 98 (5) (2006) 901–926, https://doi.org/10.1093/aob/mcl133.

[16] W.T. Koo, J.S. Jang, I.D. Kim, Metal-organic frameworks for chemiresistive sensors, Chem 5 (8) (2019) 1938–1963, https://doi.org/10.1016/j.chempr.2019.04.013.

[17] D. Jeon, M. Sagong, M.S. Kim, J.S. Nam, H. Park, I.D. Kim, Electrospun carbon nanofibers for clean energy applications: a comprehensive review, EcoMat 7 (2) (2025), https://doi.org/10.1002/eom2.12517.

[18] J.W. Jung, C.L. Lee, S. Yu, I.D. Kim, Electrospun nanofibers as a platform for advanced secondary batteries: a comprehensive review, J. Mater. Chem. A Mater. 4 (3) (2016) 703–750, https://doi.org/10.1039/c5ta06844d.

[19] J. Rosell-Llompart, J. Grifoll, I.G. Loscertales, Electrosprays in the cone-jet mode: from taylor cone formation to spray development, J. Aerosol Sci. 125 (2018) 2–31, https://doi.org/10.1016/j.jaerosci.2018.04.008.

[20] P.K. Szewczyk, U. Stachewicz, The impact of relative humidity on electrospun polymer fibers: from structural changes to fiber morphology, Adv. Colloid Interf. Sci. 286 (2020) 102315, https://doi.org/10.1016/j.cis.2020.102315.

[21] L. Zhan, X. Wang, Y. Lv, J. Deng, L. Nan, Q. Ke, S. Guan, C. Huang, Y. Ouyang, Anisotropic single-layer graphene/nanodiamond loaded PCL conduits provide biophysical cues to manipulate nerve biomechanics and bioelectric function in the restoration of nerve microenvironment, Adv. Funct. Mater. (2025), https://doi.org/10.1002/adfm.202419411.

[22] J. Deng, C. Zhai, L. Zhan, K. Zhang, T. Yang, Q. Ke, C. Huang, A. Yin, Rapid endothelialization enabled by integrating Bi-oriented topography and salvianolic acid B modification on a small-diameter fibrous graft, Compos. B Eng. (2025) 294, https://doi.org/10.1016/j.compositesb.2025.112163.

[23] S. Agarwal, A. Greiner, J.H. Wendorff, Functional materials by electrospinning of polymers, Prog. Polym. Sci. 38 (6) (2013) 963–991, https://doi.org/10.1016/j.progpolymsci.2013.02.001.

[24] I.D. Kim, A. Rothschild, Nanostructured metal oxide gas sensors prepared by electrospinning, Polym. Adv. Technol. 22 (3) (2011) 318–325, https://doi.org/10.1002/pat.1797.

[25] P. Vass, E. Szabó, A. Domokos, E. Hirsch, D. Galata, B. Farkas, B. Démuth, S. K. Andersen, T. Vigh, G. Verreck, G. Marosi, Z.K. Nagy, Scale-up of electrospinning technology: applications in the pharmaceutical industry, Wiley Interdiscip. Rev. Nanomed. Nanobiotechnol. 12 (4) (2020), https://doi.org/10.1002/wnan.1611.

[26] D. Ji, Y. Lin, X. Guo, B. Ramasubramanian, R. Wang, N. Radacsi, R. Jose, X. Qin, S. Ramakrishna, Electrospinning of nanofibres, Nat. Rev. Methods Prim. 4 (1) (2024), https://doi.org/10.1038/s43586-023-00278-z.

[27] A. Kausar, A review of filled and pristine polycarbonate blends and their applications, J. Plast. Film Sheeting 34 (1) (2018) 60–97, https://doi.org/10.1177/8756087917691088.

[28] E.V. Antonakou, D.S. Achilias, Recent advances in polycarbonate recycling: a review of degradation methods and their mechanisms, Waste Biomass Valoriz. 4 (1) (2013) 9–21, https://doi.org/10.1007/s12649-012-9159-x.

[29] M.L. Bárcenas-Argüello, T. Terrazas, S. Arias, Trichomes with crystals in the *Cephalocereus pfeiff*. areoles, Bot. Sci. 92 (3) (2014) 335–342, https://doi.org/10.17129/botsci.108.

[30] M. Kadivar, D. Tormey, G. McGranaghan, A review on turbulent flow over rough surfaces: fundamentals and theories, Int. J. Thermo. (2021) 10, https://doi.org/10.1016/j.ijft.2021.100077.

[31] E. Guen, P.O. Chapuis, N.J. Kaur, P. Klapetek, S. Gomés, Impact of roughness on heat conduction involving nanocontacts, Appl. Phys. Lett. 119 (16) (2021), https://doi.org/10.1063/5.0064244.

[32] J. Wang, Z. Zhang, R. Shi, B.N. Chandrashekar, N. Shen, H. Song, N. Wang, J. Chen, C. Cheng, Impact of nanoscale roughness on heat transport across the solid–solid interface, Adv. Mater. Interfaces 7 (4) (2020), https://doi.org/10.1002/admi.201901582.

[33] Z. Zhu, D. Wang, Y. Tian, L. Jiang, Ion/molecule transportation in nanopores and nanochannels: from critical principles to diverse functions, J. Am. Chem. Soc. 141 (22) (2019) 8658–8669, https://doi.org/10.1021/jacs.9b00086.

[34] C.L. Pai, M.C. Boyce, G.C. Rutledge, Morphology of porous and wrinkled fibers of polystyrene electrospun from dimethylformamide, Macromolecules 42 (6) (2009) 2102–2114, https://doi.org/10.1021/ma802529h.

[35] P.K. Szewczyk, D.P. Ura, S. Metwally, J. Knapczyk-Korczak, M. Gajek, M. M. Marzec, A. Bernasik, U. Stachewicz, Roughness and fiber fraction dominated wetting of electrospun fiber-based porous meshes, Polymers (Basel) 11 (1) (2019) 1–17, https://doi.org/10.3390/polym11010034.

[36] D.H. Reneker, A.L. Yarin, Electrospinning jets and polymer nanofibers, Polymer (Guildf.) 49 (10) (2008) 2387–2425, https://doi.org/10.1016/j.polymer.2008.02.002.

[37] M. Liang, X. Chen, Y. Xu, L. Zhu, X. Jin, C. Huang, Double-grooved nanofibre surfaces with enhanced anisotropic hydrophobicity, Nanoscale 9 (42) (2017) 16214–16222, https://doi.org/10.1039/c7nr05188c.

[38] U. Stachewicz, P.K. Szewczyk, A. Kruk, A.H. Barber, A. Czyrska-Filemonowicz, Pore shape and size dependence on cell growth into electrospun fiber scaffolds for tissue engineering: 2D and 3D analyses using SEM and FIB-SEM tomography, Mater. Sci. Eng. C 95 (2019) 397–408, https://doi.org/10.1016/j.msec.2017.08.076.

[39] V. Beachley, X. Wen, Effect of electrospinning parameters on the nanofiber diameter and length, Mater. Sci. Eng. C 29 (3) (2009) 663–668, https://doi.org/10.1016/j.msec.2008.10.037.

[40] D.P. Ura, J.E. Karbowniczek, P.K. Szewczyk, S. Metwally, M. Kopyściański, U. Stachewicz, Cell integration with electrospun PMMA nanofibers, microfibers, ribbons, and films: a microscopy study, Bioengineering 6 (2) (2019) 1–12, https://doi.org/10.3390/bioengineering6020041.

[41] R. Kumar, Kamakshi, M. Kumar, K. Awasthi, Functionalized Pd-decorated and aligned MWCNTs in polycarbonate as a selective membrane for hydrogen separation, Int. J. Hydrog. Energy 41 (48) (2016) 23057–23066, https://doi.org/10.1016/j.ijhydene.2016.09.008.

[42] K.A. Ross, O.H. Campanella, M.R. Okos, The effect of porosity on glass transition measurement, Int. J. Food Prop. 5 (3) (2002) 611–628, https://doi.org/10.1081/JFP-120015496.

[43] P.K. Szewczyk, D.P. Ura, U. Stachewicz, Humidity controlled mechanical properties of electrospun polyvinylidene fluoride (Pvdf) fibers, Fibers 8 (10) (2020) 1–9, https://doi.org/10.3390/fib8100065.

[44] M. Mehdikhani, L. Gorbatikh, I. Verpoest, S.V. Lomov, Voids in fiber-reinforced polymer composites: a review on their formation, characteristics, and effects on mechanical performance, J. Compos. Mater. 53 (12) (2019) 1579–1669, https://doi.org/10.1177/0021998318772152.

[45] A. Camposeo, I. Greenfeld, F. Tantussi, S. Pagliara, M. Moffa, F. Fuso, M. Allegrini, E. Zussman, D. Pisignano, Local mechanical properties of electrospun fibers correlate to their internal nanostructure, Nano Lett. 13 (11) (2013) 5056–5062, https://doi.org/10.1021/nl4033439.

[46] G. Wang, J. Zhao, L.H. Mark, G. Wang, K. Yu, C. Wang, C.B. Park, G. Zhao, Ultra-tough and super thermal-insulation nanocellular PMMA/TPU, Chem. Eng. J. 325 (2017) 632–646, https://doi.org/10.1016/j.cej.2017.05.116.

[47] U. Stachewicz, R.J. Bailey, W. Wang, A.H. Barber, Size dependent mechanical properties of electrospun polymer fibers from a composite structure, Polymer (Guildf.) 53 (22) (2012) 5132–5137, https://doi.org/10.1016/j.polymer.2012.08.064.

[48] U. Stachewicz, I. Peker, W. Tu, A.H. Barber, Stress delocalization in crack tolerant electrospun nanofiber networks, ACS Appl. Mater. Interfaces 3 (6) (2011) 1991–1996, https://doi.org/10.1021/am2002444.

[49] Y. Zhang, W. Zhu, F. Hui, M. Lanza, T. Borca-Tasciuc, M. Muñoz Rojo, A review on principles and applications of Scanning Thermal Microscopy (SThM), Adv. Funct. Mater. 30 (18) (2020), https://doi.org/10.1002/adfm.201900892.

[50] A. Moradi, P.K. Szewczyk, U. Stachewicz, Bridging a gap in thermal conductivity and heat transfer in hybrid fibers and yarns via polyimide and silicon nitride composites, Small (2023), https://doi.org/10.1002/smll.202305104.

[51] Y. Zhuge, F. Liu, Controlled preparation of polyimide/polysulfone amide (PI/PSA) porous micro-nano fiber membranes by microemulsion electrospinning for excellent thermal insulation, Eur. Polym. J. (2023) 194, https://doi.org/10.1016/j.eurpolymj.2023.112170.

[52] L. Wang, D. Ma, C. Xu, X. Gan, P. Ge, L. Zhu, X. Wang, Y. Lv, Preparation of flexible hollow TiO2 fibrous membranes for thermal-insulation applications by coaxial electrospinning, Ceram. Int. 49 (14) (2023) 22875–22881, https://doi.org/10.1016/j.ceramint.2023.04.111.

[53] O. Uyanna, H. Najafi, Thermal protection systems for space vehicles: a review on technology development, current challenges and future prospects, Acta Astronaut. 176 (2020) 341–356, https://doi.org/10.1016/j.actaastro.2020.06.047.

[54] S. Wang, C. Liu, F. Wang, X. Yin, J. Yu, S. Zhang, B. Ding, Recent advances in ultrafine fibrous materials for effective warmth retention, Adv. Fiber Mater. 5 (3) (2023) 847–867, https://doi.org/10.1007/s42765-022-00209-9.

[55] K. Swimm, S. Vidi, G. Reichenauer, H.P. Ebert, Coupling of gaseous and solid thermal conduction in porous solids, J. Non-Cryst. Solids 456 (2017) 114–124, https://doi.org/10.1016/j.jnoncrysol.2016.11.012.

[56] L. Dou, X. Cheng, X. Zhang, Y. Si, J. Yu, B. Ding, Temperature-invariant superelastic, fatigue resistant, and binary-network structured silica nanofibrous aerogels for thermal superinsulation, J. Mater. Chem. A Mater. 8 (16) (2020) 7775–7783, https://doi.org/10.1039/d0ta01092h.

[57] X.A. Zhang, S. Yu, B. Xu, M. Li, Z. Peng, Y. Wang, S. Deng, X. Wu, Z. Wu, M. Ouyang, Y. Wang, Dynamic gating of infrared radiation in a textile, Science (1979) 363 (2019) 619–623, https://doi.org/10.1126/science.aau1217.

[58] X. Li, Y. Yang, Z. Quan, L. Wang, D. Ji, F. Li, X. Qin, J. Yu, S. Ramakrishna, Tailoring body surface infrared radiation behavior through colored nanofibers for efficient passive radiative heating textiles, Chem. Eng. J. 430 (2022), https://doi.org/10.1016/j.cej.2021.133093.

[59] J.H. Kim, J.H. Ahn, J.D. Kim, D.H. Lee, S.K. Kim, J.M. Lee, Influence of silica-aerogel on mechanical characteristics of polyurethane-based composites: thermal conductivity and strength, Materials 14 (7) (2021), https://doi.org/10.3390/ma14071790.

[60] D. Zong, X. Zhang, X. Yin, F. Wang, J. Yu, S. Zhang, B. Ding, Electrospun fibrous sponges: principle, fabrication, and applications, Adv. Fiber Mater. 4 (6) (2022) 1434–1462, https://doi.org/10.1007/s42765-022-00202-2.

[61] V. Apostolopoulou-Kalkavoura, P. Munier, L. Bergström, Thermally insulating nanocellulose-based materials, Adv. Mater. 33 (28) (2021), https://doi.org/10.1002/adma.202001839.

[62] M. Wu, Z. Shao, N. Zhao, R. Zhang, G. Yuan, L. Tian, Z. Zhang, W. Gao, H. Bai, Biomimetic, knittable aerogel fiber for thermal insulation textile, Science 382 (2023) 1379–1383.

[63] Q. Peng, Y. Qin, X. Zhao, X. Sun, Q. Chen, F. Xu, Z. Lin, Y. Yuan, Y. Li, J. Li, W. Yin, C. Gao, F. Zhang, X. He, Y. Li, Superlight, mechanically flexible, thermally superinsulating, and antifrosting anisotropic nanocomposite foam based on hierarchical graphene oxide assembly, ACS Appl. Mater. Interfaces 9 (50) (2017) 44010–44017, https://doi.org/10.1021/acsami.7b14604.

[64] N. Mehra, L. Mu, T. Ji, X. Yang, J. Kong, J. Gu, J. Zhu, Thermal transport in polymeric materials and across composite interfaces, Appl. Mater. Today 12 (2018) 92–130, https://doi.org/10.1016/j.apmt.2018.04.004.

[65] Y. Jia, Z. Mao, W. Huang, J. Zhang, Effect of temperature and crystallinity on the thermal conductivity of semi-crystalline polymers: a case study of polyethylene, Mater. Chem. Phys. (2022) 287, https://doi.org/10.1016/j.matchemphys.2022.126325.

[66] J.D. Renteria, S. Ramirez, H. Malekpour, B. Alonso, A. Centeno, A. Zurutuza, A. I. Cocemasov, D.L. Nika, A.A. Balandin, Strongly anisotropic thermal conductivity of free-standing reduced graphene oxide films annealed at high temperature, Adv. Funct. Mater. 25 (29) (2015) 4664–4672, https://doi.org/10.1002/adfm.201501429.

[67] K.L. Martin, D.P. Street, C.M. Thompson, M.J.S. Parvulescu, M.B. Dickerson, Impact of the backbone structure on the rheological and thermal properties of preceramic polymer-grafted nanoparticles and derived ceramics, ACS Appl. Nano Mater. 5 (1) (2022) 446–454, https://doi.org/10.1021/acsanm.1c03278.

[68] S.C. Lee, G.R. Cunnington, Conduction and radiation heat transfer in high-porosity fiber thermal insulation, J. Thermophys. Heat Transf. 14 (2) (2000) 121–136, https://doi.org/10.2514/2.6508.

[69] U. Stachewicz, F. Hang, A.H. Barber, Adhesion anisotropy between contacting electrospun fibers, Langmuir 30 (23) (2014) 6819–6825, https://doi.org/10.1021/la5004337.

[70] Y. Guo, K. Ruan, X. Shi, X. Yang, J. Gu, Factors affecting thermal conductivities of the polymers and polymer composites: a review, Compos. Sci. Technol. 193 (2020), https://doi.org/10.1016/j.compscitech.2020.108134.

[71] H. Liu, X. Zhao, Thermal conductivity analysis of high porosity structures with open and closed pores, Int. J. Heat Mass Transf. (2022) 183, https://doi.org/10.1016/j.ijheatmasstransfer.2021.122089.

[72] J. Knapczyk-Korczak, P.K. Szewczyk, K. Berniak, M.M. Marzec, M. Frąc, W. Pichór, U. Stachewicz, Flexible and thermally insulating porous materials utilizing hollow double-shell polymer fibers, Adv. Sci. (2024) 2404154, https://doi.org/10.1002/advs.202404154.

[73] M. Obori, D. Suh, S. Yamasaki, T. Kodama, T. Saito, A. Isogai, J. Shiomi, Parametric model to analyze the components of the thermal conductivity of a cellulose-nanofibril aerogel, Phys. Rev. Appl. 11 (2) (2019), https://doi.org/10.1103/PhysRevApplied.11.024044.

[74] Z. Said, L.S. Sundar, A.K. Tiwari, H.M. Ali, M. Sheikholeslami, E. Bellos, H. Babar, Recent advances on the fundamental physical phenomena behind stability, dynamic motion, thermophysical properties, heat transport, applications, and challenges of nanofluids, Phys. Rep. 946 (2022) 1–94, https://doi.org/10.1016/j.physrep.2021.07.002.

[75] J. Gu, K. Ruan, Breaking through bottlenecks for thermally conductive polymer composites: a perspective for intrinsic thermal conductivity, interfacial thermal resistance and theoretics, Nano Lett. 13 (1) (2021), https://doi.org/10.1007/s40820-021-00640-4.

[76] S. Wang, C. Zhu, F. Wang, J. Yu, S. Zhang, B. Ding, Ultralight and superelastic curly micro/nanofibrous aerogels by direct electrospinning enable high-performance warmth retention, Small (2023), https://doi.org/10.1002/smll.202302835.

[77] H.L. Paul, K.R. Diller, Comparison of thermal insulation performance of fibrous materials for the advanced space suit, J. Biomech. Eng. 125 (5) (2003) 639–647, https://doi.org/10.1115/1.1611885.

[78] H. Zhong, Y. Li, P. Zhang, S. Gao, B. Liu, Y. Wang, T. Meng, Y. Zhou, H. Hou, C. Xue, Y. Zhao, Z. Wang, Hierarchically Zhollow microfibers as a scalable and effective thermal insulating cooler for buildings, ACS Nano 15 (6) (2021) 10076–10083, https://doi.org/10.1021/acsnano.1c01814.

[79] M. Kadivar, D. Tormey, G. McGranaghan, A review on turbulent flow over rough surfaces: fundamentals and theories, Int. J. Thermo. (2021) 10, https://doi.org/10.1016/j.ijft.2021.100077.

[80] D. Noto, J.A. Letelier, H.N. Ulloa, M. Manga, Plume-scale confinement on thermal convection, PNAS 121 (2024) 20, https://doi.org/10.1073/pnas.

[81] D. Surblys, Y. Kawagoe, M. Shibahara, T. Ohara, Molecular dynamics investigation of surface roughness scale effect on interfacial thermal conductance at solid-liquid interfaces, J. Chem. Phys. 150 (11) (2019), https://doi.org/10.1063/1.5081103.

[82] L.D. Hung Anh, Z. Pásztory, An overview of factors influencing thermal conductivity of building insulation materials, J. Build. Eng. 44 (2021), https://doi.org/10.1016/j.jobe.2021.102604.

[83] G.I. Saidal', P.V. Kopchenko, K.V. Plastinin, B.A. Levin, Reinforced structures of cryoinsulation based on the synthetic rubber K-Flex, Chem. Pet. Eng. 39 (9) (2003) 539–542.

[84] X. Ding, H. Xun, Q. Cao, X. Zhang, H. Zhou, H. Niu, High-comfort, ultrathin air-layer nanofiber composite membrane for thermal insulation in complex environments, Sustain. Mater. Technol. (2025) 44, https://doi.org/10.1016/j.susmat.2025.e01382.

[85] C. Xu, C. Yue, Y. Yao, Y. Yu, L. Li, X. Liu, 3D cotton-like phase change fibers via electrospinning for thermal management of textile, J. Energy Storage (2024) 84, https://doi.org/10.1016/j.est.2024.110991.

[86] H. Wang, Y. Zhang, H. Niu, L. Wu, X. He, T. Xu, N. Wang, Y. Yao, An electrospinning–electrospraying technique for connecting electrospun fibers to enhance the thermal conductivity of boron nitride/polymer composite films, Compos. B Eng. (2022) 230, https://doi.org/10.1016/j.compositesb.2021.109505.

[87] Z. Wei, X. Kong, J. Cheng, H. Zhou, J. Yu, S. Lu, Constructing a "Pearl-Necklace-Like" architecture for enhancing thermal conductivity of composite films by electrospinning, Compos. Commun. 29 (2022), https://doi.org/10.1016/j.coco.2021.101036.

[88] C. Pan, F. Wu, G. Fan, Y. Long, H. Yang, G. Yang, X. Li, A multifunctional flexible composite film with excellent insulation flame retardancy, thermal management and solar-thermal conversion properties based on CNF-modified mica/electrospun fibrous networks structure, Sol. Energy Mater. Sol. Cells (2023), https://doi.org/10.1016/j.solmat.2023.112530.

[89] Y. Zhang, S. Yang, Q. Zhang, Z. Ma, Y. Guo, M. Shi, H. Wu, S. Guo, Constructing interconnected asymmetric conductive network in TPU fibrous film: achieving low-reflection electromagnetic interference shielding and surperior thermal conductivity, Carbon N. Y. 206 (2023) 37–44, https://doi.org/10.1016/j.carbon.2023.01.043.

[90] J. Yang, T. Zhang, S. Wang, S. Wang, H. Ding, J. Xie, D. Xu, Q. Huang, C. Liu, Preparation of flexible phase change fiber membrane for thermal insulation based on electrostatic spinning process, Vacuum 238 (2025), https://doi.org/10.1016/j.vacuum.2025.114214.

[91] J. Wu, M. Wang, L. Dong, C. Zhu, J. Shi, H. Morikawa, Ultraflexible, breathable, and form-stable phase change fibrous membranes by green electrospinning for personal thermal management, ACS Sustain. Chem. Eng. 10 (24) (2022) 7873–7882, https://doi.org/10.1021/acssuschemeng.2c00189.

[92] Zhao, G. Zhi, R. Ma, Y. Yin, Thermal conductivity hydroxylated boron nitride/polyurethane/polyvinyl alcohol composite nanofiber film prepared by electrospinning, Macromol. Chem. Phys. (2024), https://doi.org/10.1002/macp.202400365.

[93] H. Zheng, G. Xu, K. Wu, L. Feng, R. Zhang, Y. Bao, H. Wang, K. Wang, Z. Qu, J. Shi, Highly intrinsic thermally conductive electrospinning film with intermolecular interaction, J. Phys. Chem. C 125 (39) (2021) 21580–21587, https://doi.org/10.1021/acs.jpcc.1c04919.

[94] V. Wable, P.K. Biswas, R. Moheimani, N. Aliahmad, P. Omole, A.P. Siegel, M. Agarwal, H. Dalir, Engineering the electrospinning of MWCNTs/epoxy nanofiber scaffolds to enhance physical and mechanical properties of CFRPs, Compos. Sci. Technol. 213 (2021), https://doi.org/10.1016/j.compscitech.2021.108941.

[95] V. Rahmanian, T. Pirzada, E. Barbieri, S. Iftikhar, F. Li, S.A. Khan, Mechanically robust, thermally insulating and photo-responsive aerogels designed from sol-gel electrospun PVP-TiO2 nanofibers, Appl. Mater. Today (2023) 32, https://doi.org/10.1016/j.apmt.2023.101784.

[96] Z. Wang, L. Fan, R. Li, Y. Xu, Q. Fu, Preparation of polymer composites with high thermal conductivity by constructing a "double thermal conductive network" via electrostatic spinning, Compos. Commun. 36 (2022), https://doi.org/10.1016/j.coco.2022.101371.

[97] W. Yang, Y. Zhan, Q. Feng, A. Sun, H. Dong, Flexible H-BN/fluorinated poly (arylene ether nitrile) fibrous composite film with low dielectric constant and high thermal conductivity fabricated via coaxial electrospinning hot-pressing technique, Colloids Surf. A Physicochem. Eng. Asp. (2022) 649, https://doi.org/10.1016/j.colsurfa.2022.129455.

[98] Y. Ma, J. Shen, X. Sheng, Y. Chen, Y. Ma, T. Li, X. Sheng, A "net-ball" structure fiber membrane with electro-/photo-thermal heating and phase change synchronous temperature regulation capacity via electrospinning, Sol. Energy Mater. Sol. Cells 276 (2024), https://doi.org/10.1016/j.solmat.2024.113078.

[99] L. An, M. Di Luigi, J. Tan, D. Faghihi, S. Ren, Flexible percolation fibrous thermal insulating composite membranes for thermal management†, Mater. Adv. 4 (1) (2023) 284–290, https://doi.org/10.1039/d2ma00915c.

[100] X. Cheng, Y.T. Liu, Y. Si, J. Yu, B. Ding, Direct synthesis of highly stretchable ceramic nanofibrous aerogels via 3D reaction electrospinning, Nat. Commun. 13 (1) (2022), https://doi.org/10.1038/s41467-022-30435-z.

[101] B. Zhang, Z. Tong, Y. Pang, H. Xu, X. Li, H. Ji, Design and electrospun closed cell structured SiO2 nanocomposite fiber by hollow SiO2/TiO2 spheres for thermal insulation, Compos. Sci. Technol. 218 (2022), https://doi.org/10.1016/j.compscitech.2021.109152.

[102] Z. Xu, Y. Liu, Q. Xin, J. Dai, J. Yu, L. Cheng, Y.T. Liu, B. Ding, Ceramic meta-aerogel with thermal superinsulation up to 1700 °C constructed by self-crosslinked nanofibrous network via reaction electrospinning, Adv. Mater. 36 (32) (2024), https://doi.org/10.1002/adma.202401299.

[103] M. Yang, Y. Lixia, Z. Chen, W. Qiong, Y. Wang, T. Liu, M. Li, Flexible electrospun strawberry-like structure SiO2 aerogel nanofibers for thermal insulation, Ceram. Int. 49 (6) (2023) 9165–9172, https://doi.org/10.1016/j.ceramint.2022.11.076.

[104] X. Liao, J. Denk, T. Tran, N. Miyajima, L. Benker, S. Rosenfeldt, S. Schafföner, M. Retsch, A. Greiner, G. Motz, S. Agarwal, Extremely low thermal conductivity and high electrical conductivity of sustainable carbonceramic electrospun nonwoven materials, Sci. Adv. (13) (2023), https://doi.org/10.1126/sciadv.ade6066.

[105] B. Zhao, J. Huang, Q. Wang, H. Huang, Q. Chen, Fabrication of ultra-fine flexible Y2Si2O7 fibrous membranes for thermal insulation by electrospinning, Ceram. Int. 49 (22) (2023) 35722–35729, https://doi.org/10.1016/j.ceramint.2023.08.251.

[106] J. Li, Q. Fang, L. Zhang, Y. Liu, The Effect of rough surface on nanoscale high speed grinding by a molecular dynamics simulation, Comput. Mater. Sci. 98 (2015) 252–262, https://doi.org/10.1016/j.commatsci.2014.10.069.

[107] S. Singh, S.K. Singh, H.S. Mali, R. Dayal, Numerical investigation of heat transfer in structured rough microchannels subjected to pulsed flow, Appl. Therm. Eng. (2021) 197, https://doi.org/10.1016/j.applthermaleng.2021.117361.
[108] B.J.R. Davidsson, H. Rickman, Surface roughness and three-dimensional heat conduction in thermophysical models, Icarus 243 (2014) 58–77, https://doi.org/10.1016/j.icarus.2014.08.039.
[109] P. Wiśniewska, J.T. Haponiuk, X. Colom, M.R. Saeb, Green approaches in rubber recycling technologies: present status and future perspective, ACS Sustain. Chem. Eng. 11 (24) (2023) 8706–8726, https://doi.org/10.1021/acssuschemeng.3c01314.
[110] Y. Liu, X.B. Lu, Chemical recycling to monomers: industrial bisphenol-A-polycarbonates to novel aliphatic polycarbonate materials, J. Polym. Sci. 60 (24) (2022) 3256–3268, https://doi.org/10.1002/pol.20220118.
[111] S. Ramakrishna, R. Jose, Principles of materials circular economy, Matter 5 (12) (2022) 4097–4099, https://doi.org/10.1016/j.matt.2022.11.009.
[112] V.T. Morgan, The overall convective heat transfer from smooth circular cylinders, Adv. Heat Tran. 11 (1975) 199–264, https://doi.org/10.1016/S0065-2717(08)70075-3.